Emplacement and flow dynamics in a small volcanic dyke swarm: The example of Mount Calanna (Etna, Italy)

Rasia Shajahan, Andrew Harris, Sara Mana, Eugenio Nicotra, Claudio Robustelli Test, Benjamin van Wyk de Vries, Elena Zanella

Journal of Volcanology and Geothermal Research 449 (2024) 108069

Contents lists available at ScienceDirect

Journal of Volcanology and Geothermal Research

journal homepage: www.journals.elsevier.com/journal-of-volcanology-and-geothermal-research

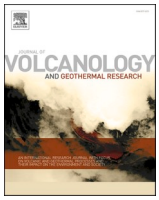

Emplacement and flow dynamics in a small volcanic dyke swarm: The example of Mount Calanna (Etna, Italy)

Rasia Shajahan [a,*], Andrew Harris [b], Sara Mana [c], Eugenio Nicotra [d], Claudio Robustelli Test [a], Benjamin Van Wyk de Vries [b], Elena Zanella [a]

[a] Dipartimento di Scienze della Terra, Università degli Studi di Torino, Via Valperga Caluso 35, 10125 Torino, Italy
[b] Université Clermont Auvergne, Laboratoire Magmas et Volcans, 63000 Clermont-Ferrand, France
[c] Salem State University, Department of Geological Sciences, 352 Lafayette Street Salem, MA 01970, United States of America
[d] Università della Calabria, Dipartimento di Biologia Ecologia e Scienze della Terra, Via P. Bucci 15/B, 87036 Rende (CS), Italy

ARTICLE INFO

Keywords:
AMS
Dyke swarm
Etna
Petrographic fabric
Magma flow
Shallow plumbing system

ABSTRACT

The emplacement mechanism and flow dynamics of small dyke swarms associated with monogenetic eruptive centres are less well studied than those of large swarms associated with shield volcanoes and flood basalts. This is due to their limited exposure and ease of reworking by later events. However, the study of small dykes helps to better constrain the forces controlling dyke propagation and thus reconstruct the emplacement history of the volcanic system. This study presents a multidisciplinary analysis of Mount Calanna (Mount Etna, Italy) where we sampled a total of 11 dykes among the two groups: 1) sub-vertical dykes from the lower part of the system, and 2) sub-horizontal dykes from the upper part. To infer the magma flow direction, we used Anisotropy of Magnetic Susceptibility (AMS) and compared the results to the Shape Preferred Orientation (SPO) of the plagioclase crystal fabric. To quantify the relative timing of dyke emplacement, and to characterise the magma plumbing system, we also used the palaeomagnetic and geochemical signature of the sampled dykes.

The fabric analysis highlights a NE-SW flow direction in the sub-vertical dykes, and a NE-SW and NW-SE direction in the sub-horizontal dykes. Dykes emplaced at the lowest levels in the swarm show sub-vertical to inclined magma flow, whereas those towards the top of the Mount Calanna show inclined to sub-horizontal flow. The combined structural and geochemical analyses suggest the Mount Calanna swarm is a coherent intrusive complex associated with a phase of activity of Ancient Alkaline centre (AAC), with Mount Calanna representing an example of the uppermost portion of a shallow plumbing system in which intrusion orientations are controlled by regional tectonics.

1. Introduction

Dykes and sills are planar intrusions that can connect multiple magma reservoirs located at different depths and/or allow magma ascent towards the surface (e.g., Gudmundsson, 1990; Gudmundsson, 2002; Magee et al., 2018). Within magmatic plumbing systems, magma moves between storage zones, and into the volcanic construct, via connecting structures (i.e., dykes and sills); which sometimes feed eruptive activity and sometimes remain intrusive (Francis, 1993). The orientation, emplacement depth and magma propagation of the resulting dyke or sill depend primarily on the stress state in the crust and within the volcanic edifice as well as on magma buoyancy (e.g., Acocella and Neri, 2009; Woo and Kilburn, 2010; Daniels and Menand, 2015; Rivalta et al., 2015; Mantiloni et al., 2023). This stress state of volcanic edifice is controlled by the stress-generating mechanisms, such as gravitational loading due to the gross morphology of the volcano (McGuire and Pullen, 1989; Maccaferri et al., 2017; Davis et al., 2021), the magma reservoir (Roman and Jaupart, 2014; Pansino and Taisne, 2019), and the emplacement of the dykes themselves (Hamling et al., 2010; Daniels and Menand, 2015). Thus, studying emplacement of, and magma flow in, dykes and sills is essential in understanding how feeder systems develop, as well as flow dynamics within that system (e.g., Wiegand et al., 2017; Minakov et al., 2018; Das and Mallik, 2020; Datta et al., 2023).

The direction of magma flow in dykes and sills can be investigated using a variety of approaches, including mineral alignment, dyke

* Corresponding author.
E-mail address: rasia.shajahan@unito.it (R. Shajahan).

https://doi.org/10.1016/j.jvolgeores.2024.108069
Received 4 September 2023; Received in revised form 11 March 2024; Accepted 2 April 2024
Available online 4 April 2024

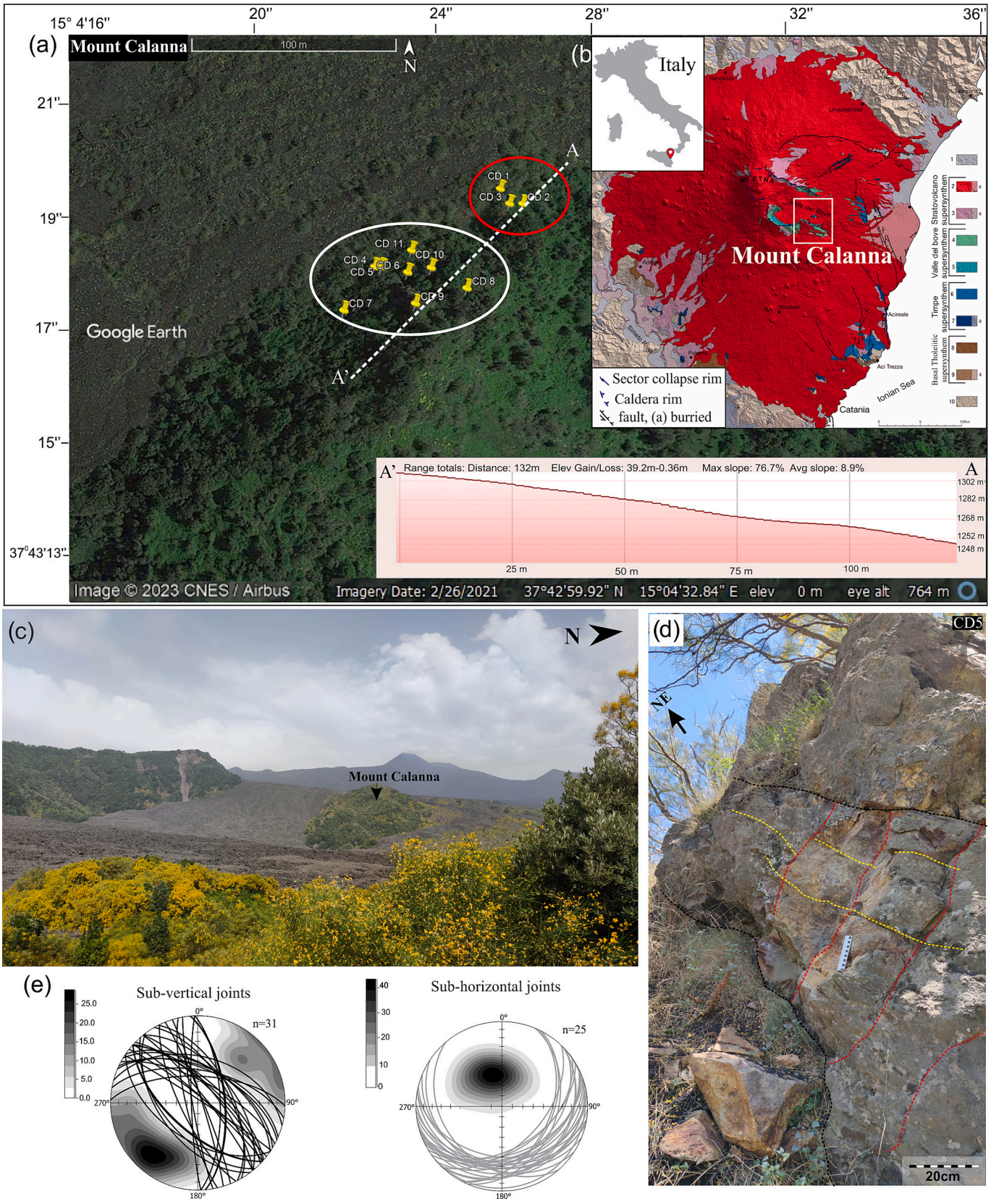

Fig. 1. a) Google Earth image showing the spatial distribution of sampled dykes. The two circles outline the sub-vertically (red circle) and sub-horizontally (white circle) emplaced dykes and the left bottom inset shows the elevation profile along A-A' transect. b) Digital elevation model (DEM) of Mount Etna along with the position of Mount Calanna (modified after Branca et al., 2011). c) Field photo of Mount Calanna surrounded by recent lava flow of Mount Etna summit eruption (1991–1992). The black dotted square shows the area of sampling. (d) Field photo of a sub-horizontal dyke (CD 5) showing the contact with country rock (black dotted lines) and the subvertical (red dotted lines) and sub-horizontal (yellow dotted lines) joints. (e) Lower hemisphere equal-area projections of all measured joints orientation with the contour diagrams of their pole.

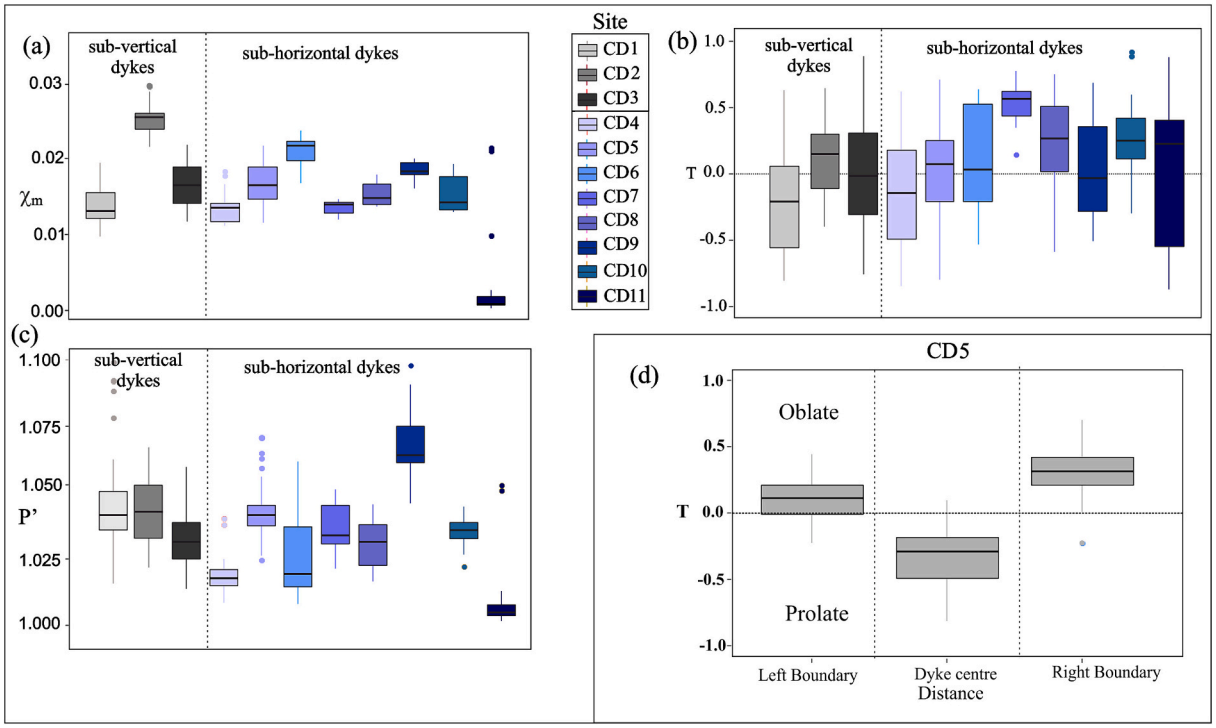

Fig. 2. Box plots of a) mass susceptibility, b) shape parameter and c) corrected degree of anisotropy for the two groups of dykes. d) Box plot showing the variation of shape parameter between boundaries and centre for dyke CD5 (sub-horizontal dyke).

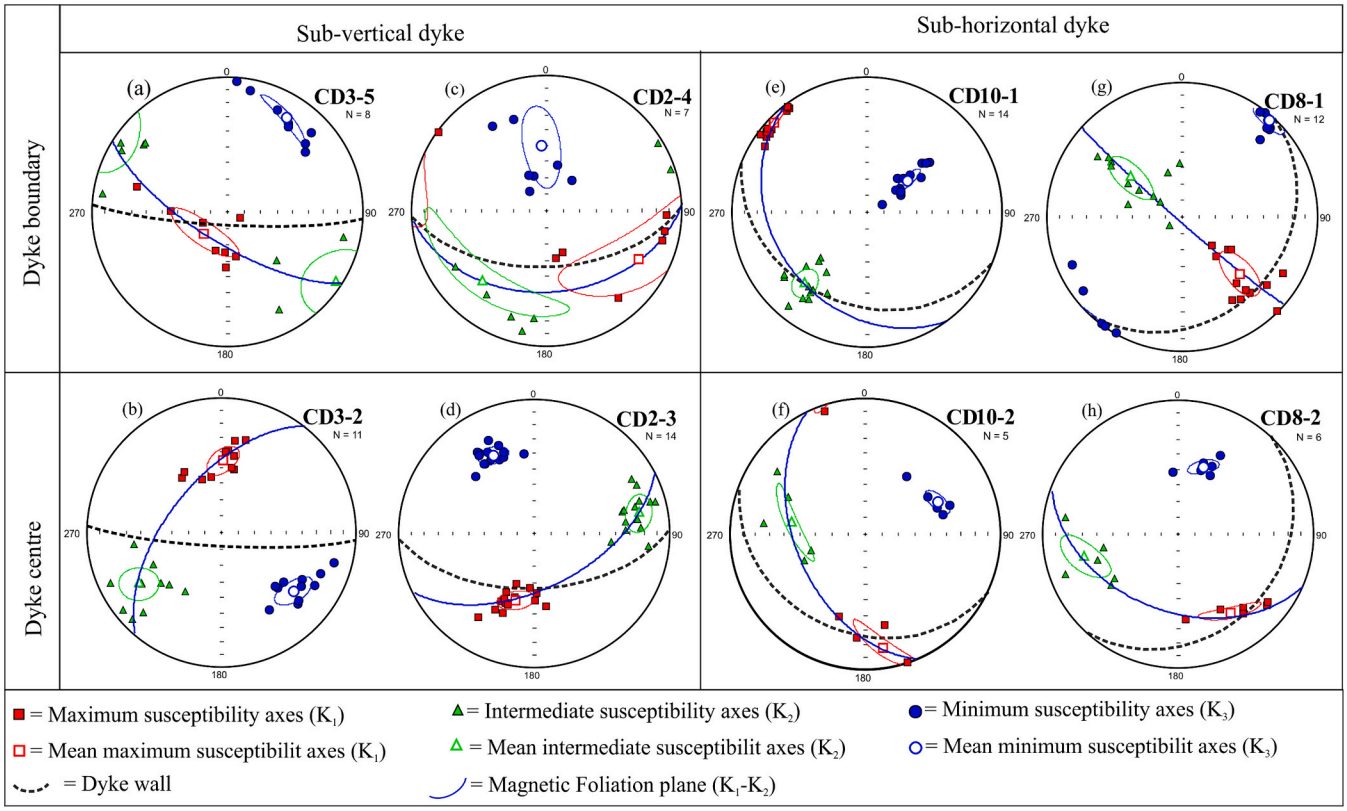

Fig. 3. Equal-area projection of the three susceptibility axes, their mean values with associated confidence limits, and magnetic foliation plane (blue line), for sub-vertical (on the left) and sub-horizontal (on the right) dykes. The dotted black line represents the orientation of the dyke wall.

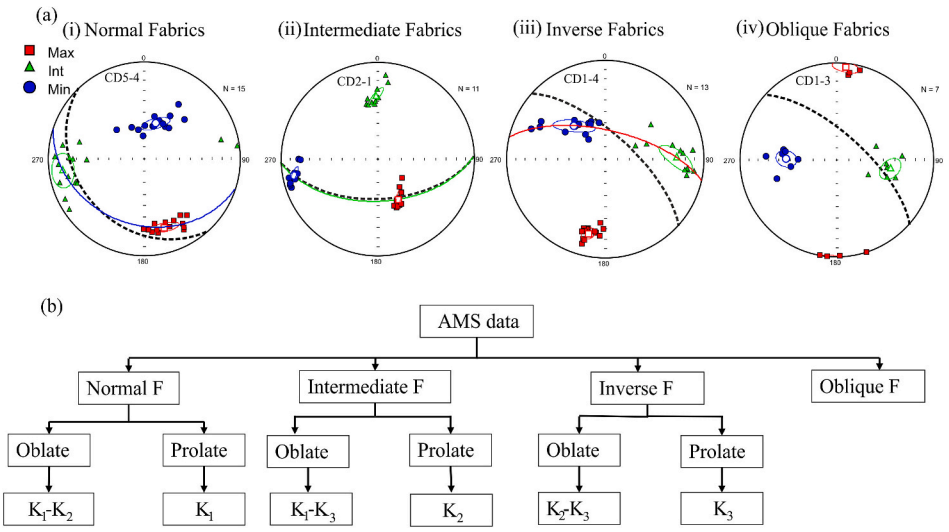

Fig. 4. (a) Examples of four different types of fabrics, namely, Normal, Intermediate, Inverse, and Oblique fabrics respectively. The dotted lines show the orientation of the dyke plane; (b) flow chart showing the proposed approach for AMS flow fabric interpretation.

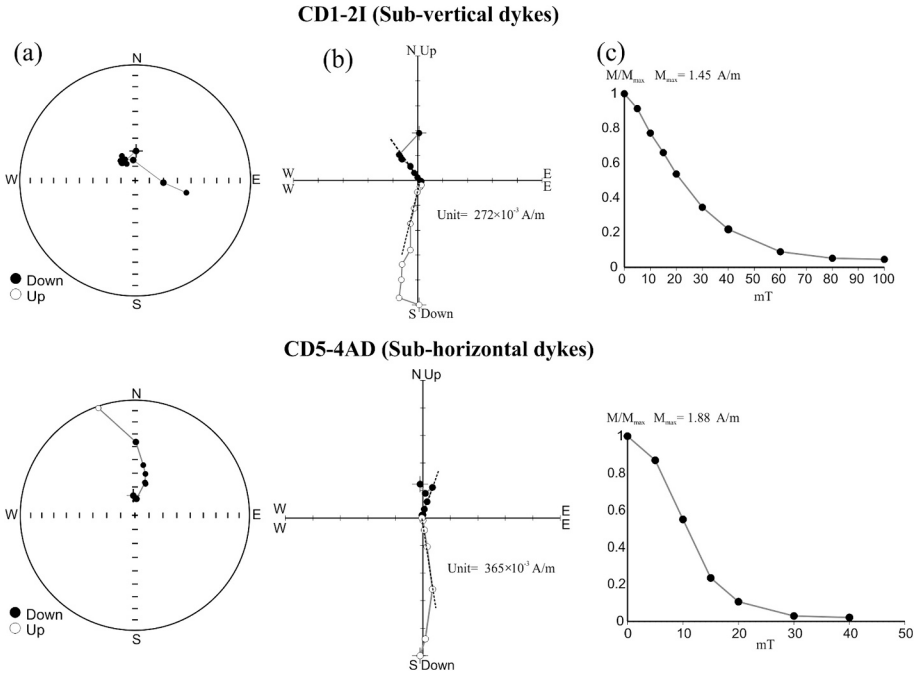

Fig. 5. Examples of alternating field (AF) demagnetization behaviour of a sub-vertical dyke (top) and a sub-horizontal dyke (bottom). (a) Stereographic projection of magnetic direction; (b) Zijderveld diagrams with solid and open data showing declination and apparent inclination, respectively. Black straight lines are the best-fitted direction interpreted by PCA; (c) Intensity decay curve of remanent magnetization as a function of the applied field.

segmentation, preferred orientation of plagioclase, magnetic fabric and vesicle deformation (Coward, 1980; Tarling and Hrouda, 1993; Archanjo and Launeau, 2004; Geshi, 2008). Among these, analysis of magnetic fabric is one of the most commonly used methods (see Martin et al., 2019 for review), where anisotropy of magnetic susceptibility (AMS) has been used to examine magnetic fabrics and flow directions in both dykes (Khan, 1962; Chadima et al., 2009; Delcamp et al., 2015; Wiegand et al., 2017; Otmane et al., 2018; Das et al., 2019; Das and Mallik, 2020; Trippanera et al., 2020) and sills (Dragoni et al., 1997; Hoyer and Watkeys, 2017; Schmiedel et al., 2021). Anisotropy of magnetic susceptibility is a powerful rock property used to quantitatively characterise the rock fabric. The magnetic property of minerals in a rock to tend to be aligned in a common direction results in magnetic anisotropy, which is determined by the overall orientations and the shape and crystallography of each mineral. This resulting magnetic anisotropy provides information for the development of emplacement models and for understanding of post-emplacement processes of dykes and lava flows (e.g., Khan, 1962; Chadima et al., 2009; Trippanera et al., 2020).

Most AMS studies on dykes have focused on large dyke swarms, such as those of the Mackenzie (Ernst and Baragar, 1992) and Deccan (Ray et al., 2007) flood basalts, as well as in Iceland (Eriksson et al., 2015) and Rio Cearfi-Mirim (Archanjo and Launeau, 2004). In contrast, small dyke swarms at single eruptive centres (stratovolcanoes), are poorly studied. This is mostly due to lack of outcrop, so that the number of dykes and/or sills available for sampling is small.

To assess dyke mechanisms at a single eruptive centre, we thus

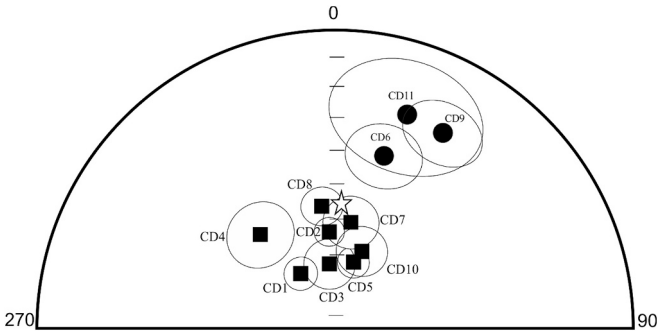

Fig. 6. Site mean direction of ChRM of the sampled dykes with their α_{95} confidence limits. Black square and circle represents the primary and secondary cluster of ChRM respectively. The star is the Geocentric Axial Dipole (GAD) direction at Mount Calanna geographic coordinates.

conducted a magnetic fabric, palaeomagnetic, rock magnetic, geochemical, and textural study of the dyke swarm at Mount Calanna (Mount Etna, Italy). We combine these data to provide a view of dyke emplacement mechanisms and to propose an approach to interpret magma flow direction in dykes using AMS. Finally, we combine AMS and Shape Preferred Orientation (SPO) data to build a dyke emplacement model for the sub-vertically and sub-horizontally emplaced dykes of Mount Calanna.

2. Geological setting

2.1. Mount Etna

Mount Etna is a Quaternary stratovolcano located on the eastern coast of Sicily (Southern Italy) and over the front of the Apennine - Maghrebian thrust (Gvirtzman and Nur, 1999). Volcanic activity began about 600 ka with the submarine emission of tholeiitic products, which now outcrop on Etna's southeastern (Aci Trezza Synthem) and southwestern (Adrano Synthem) flanks (Branca et al., 2008). Around 220 ka volcanism focused to the west of the present-day eastern coastline, with the formation of the Timpe fissure system (Acireale Synthem) and a shift towards Na-alkaline transitional compositions (Tanguy et al., 1997). Volcanic activity related to central-conduit systems began about 130 ka with construction of Mount Calanna (St. Alfio Synthem), which had a Na-alkaline affinity and represented the first of a series of volcanic centres that developed on the lower eastern flanks (cf. Branca et al., 2011), this being the Valle del Bove Synthem (120–65 ka). The volcanic activity shifted westward over time, reaching the present-day position around 65 ka with the onset of the Ellittico (Concazze Synthem). Development of the Ellittico lasted until 15 ka and ended with a caldera collapse (cf. Nicotra et al., 2010; Nicotra and Viccaro, 2012). Recent activity (Mongibello volcano, Il Piano Synthem) resumed after a short quiescence. Eruptive styles have been quite varied, with alternating cycles of Strombolian to Plinian eruptions followed by long periods of effusive activity (Hughes, 1990).

2.2. Mount Calanna

Mount Calanna has an area of about 0.7 km^2, a peak at 1314 m.s.l., and is located on the southeastern flank of Mount Etna (Figs. 1a-c). Mount Calanna or the Calanna Formation (Branca et al., 2008) consists of a succession of highly altered or "and" faulted lava flows and breccia cut by tens of dykes (Romano and Sturiale, 1975; Romano, 1982; Ferlito and Nicotra, 2010; Nicotra et al., 2011). Mount Calanna is surrounded by historic lava flows, including those of 1950–51 and 1991–93 (Fig. 1c), and its easternmost tip is covered by a small porphyritic hawaiitic lava flow emitted from a 210°N oriented dyke related to a recent (but undated) lateral eruption of Mongibello (Ferlito and Nicotra, 2010).

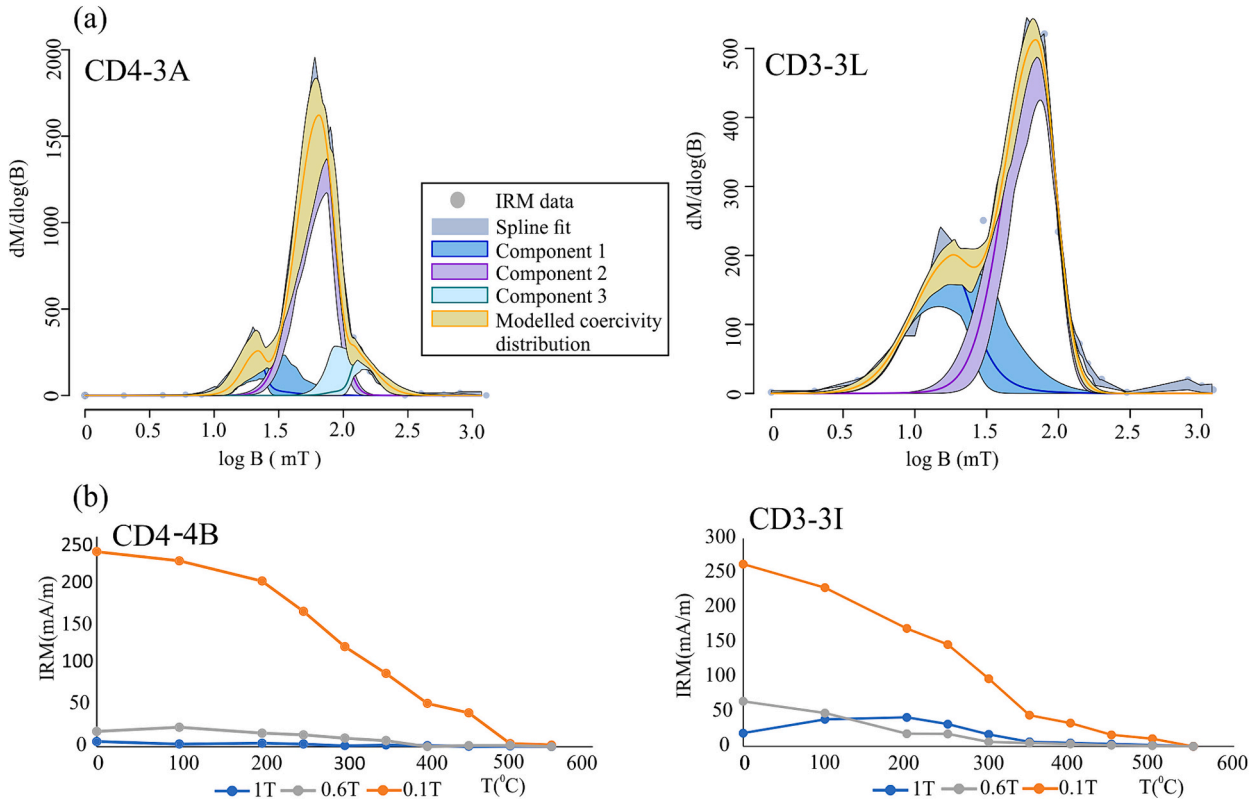

Fig. 7. (a) Coercivity spectra and unmixing curve of isothermal remanence (IRM) acquisition curves for two representative specimens (Maxbauer et al., 2016) (b) Thermal demagnetization of three-axial IRM imparted at 0.1 T,0.6 T and 1 T (Lowrie, 1990).

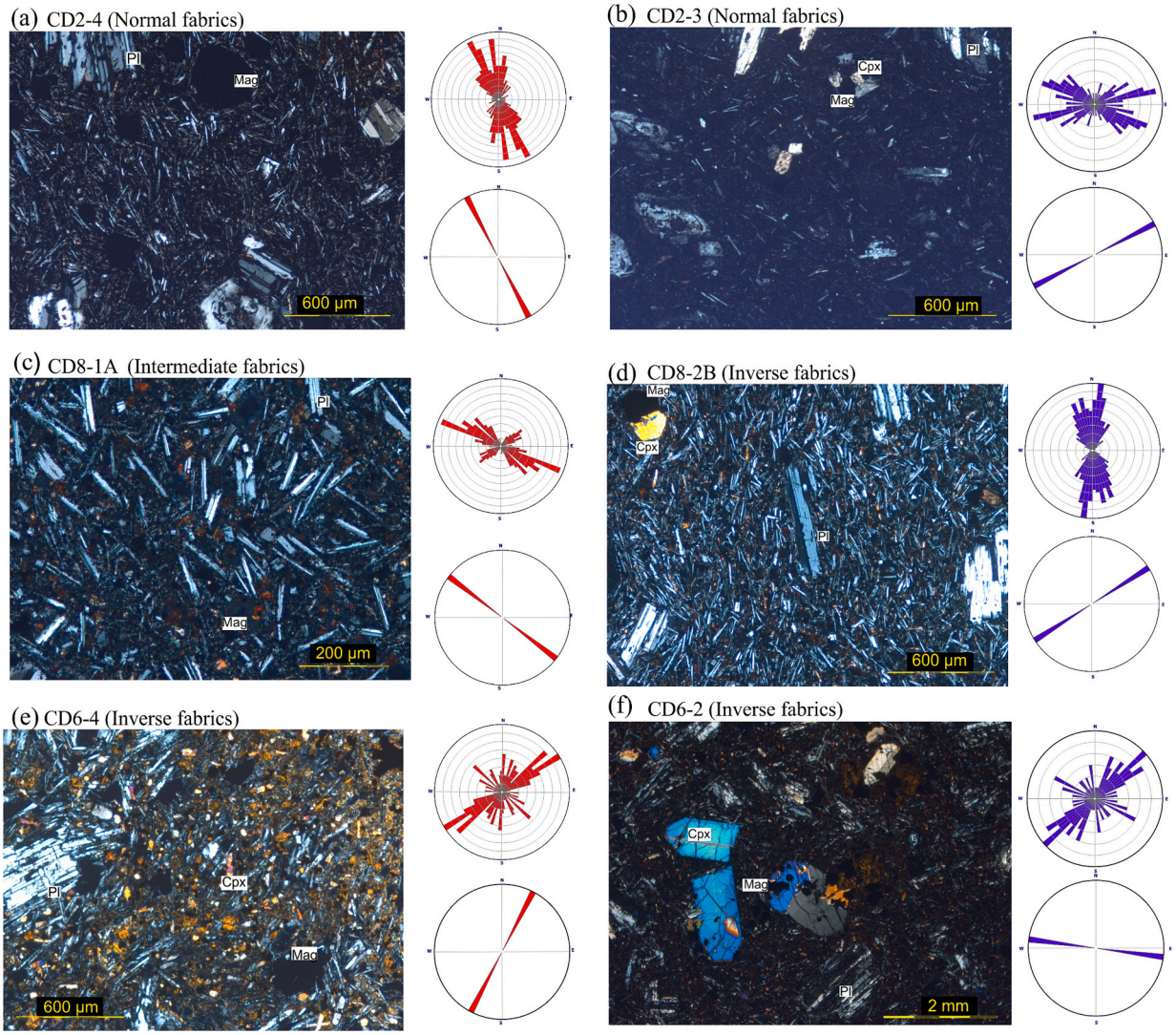

Fig. 8. Reflected-light micrograph image of three representative dykes. The top Rose diagram shows the orientation distribution of plagioclase and pyroxene from the dyke walls (red) and dyke centre (blue) obtained with the software program ImageJ (Rasband, 2012). The bottom Rose diagram represents the flow direction obtained from AMS analysis. (For interpretation of the references to colour in this figure legend, the reader is referred to the web version of this article.)

Initially, Mount Calanna was interpreted as the remains of the Ancient Alkaline Centre Phase (corresponding to the Timpe and Valle del Bove Supersynthem; Klerkx, 1970; Romano, 1982). Later, McGuire (1982) proposed that Mount Calanna represented a volcanic neck that was later dissected by dykes. Instead, Ferrari et al. (1989) defined Mount Calanna as a succession of stacked-up thrust faults, formed by gravitational spreading of the volcanic edifice. However, Ferlito and Nicotra (2010) found no compressional structures at Mount Calanna, but confirmed the presence of tens of dykes and normal faults. Based on structural and geochemical analyses, Ferlito and Nicotra (2010) interpreted Mount Calanna as an intrusive complex that was part of the uppermost portion of a shallow plumbing system.

Due to the high alteration of Mount Calanna, absolute dating is a challenge (Ferrari et al., 1989; Gillot et al., 1994). However, $^{40}Ar/^{39}Ar$ dating of rocks of Val Calanna, a small valley south of Mount Calanna, yielded an age of 128.7 ± 3.8 ka (Branca et al., 2008; De Beni et al., 2011). This locates Mount Calanna at the base of the St. Alfio Synthem, places the intrusive system at base of the Mount Etna edifice and, thus, during the central conduit-related volcanic activity. The transitional affinity of its products (Corsaro and Cristofolini, 1997; Branca et al., 2008) suggest that Mount Calanna a structure related to the transition of volcanic products of Mount Etna from tholeiitic to alkaline during the beginning of Etna's growth (Ferlito and Nicotra, 2010).

Mount Calanna comprises about 200 dykes (Fig. 1c) belonging to the Na-alkaline suite of Etna's succession, while the host rock has volcanic origin (Tanguy et al., 1997; Ferlito and Nicotra, 2010). The dyke swarm has an intensity of intrusion (i.e., volume ratio between intruded dykes and host rock) of about 40% (Ferlito and Nicotra, 2010). Ferlito and Nicotra (2010) grouped the dykes into two classes: i) *E*-W oriented and altered, which comprise 90% of the dykes, and ii) ENE-WSW oriented and unaltered, which were interpreted as the feeder systems for the subsequent eruptive events. Both the host rock and altered dyke-group have been reworked by E-W striking faults, intrusion by unaltered dykes, and dissection by joints (Figs. 1d-e). The joints follow the same orientation as major volcano-tectonic structures in the area, which strike NNW-SSE, ESE-WNW, WSW-ENE, and NE-SW, and which are controlled by the regional tectonics (Lo Giudice et al., 1982; Monaco et al., 1997, 2005).

3. Sampling and laboratory procedures

For sampling, we focused on the northern part of Mount Calanna (Fig. 1a). The southern and eastern parts of Mount Calanna are not exposed because of vegetation cover and airfall from recent eruptions.

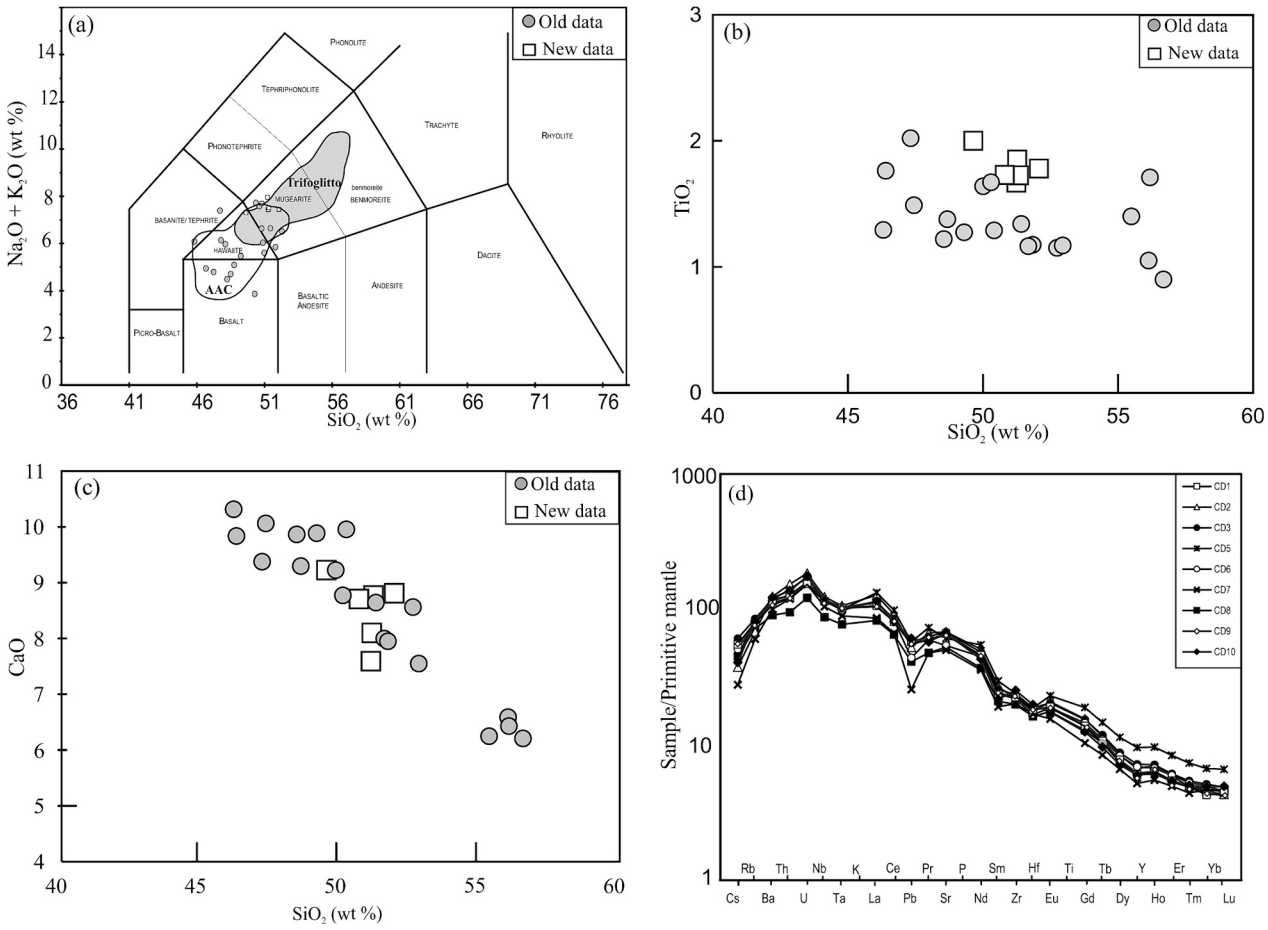

Fig. 9. (a) Total alkali silica diagram for the Mount Calanna dykes and volcanic rock belongs to AAC (old data from Cristofolini et al., 1991) (modified after Le Maitre et al. (2002)). (b) and (c) Binary diagram from TiO_2 and FeO* plotted against SiO_2 with new data and old (Cristofolini et al., 1991). (d) Trace element spider diagram normalised to primitive mantle (McDonough and Sun, 1995) for the Mount Calanna dykes.

We sampled 11 dykes, three of which were from the lower part of Mount Calanna (CD1, CD2, and CD3), and eight of which were located in top part of Mount Calanna (CD4 – CD11) (Fig. 1a). Sampled dykes were continuous, >0.5 m thick, and samples were collected from both the marginal and central parts of each dyke.

We collected 45 hand samples, oriented by both magnetic and solar compass. These were subsequently cored and cut into 254 cylindrical specimens (diameter = 25 mm, height = 22 mm), 34 mini-cores (diameter = 10 mm, height = 20 mm), and 26 equidimensional chips (size ~1 × 1 cm). The inner part of each dyke, being the less weathered portion, was sampled for geochemical analysis. Due to intense alteration, fresh 'unaltered' samples could be collected only from nine dykes.

3.1. Magnetic measurements

All magnetic measurements were performed at the Alpine Laboratory of Paleomagnetism (Italy). First, magnetic susceptibility (K_m) and its anisotropy (AMS) were measured to study the dyke flow direction and emplacement mode (sub-vertical and sub-horizontal).

AMS measurements were performed on all samples (standard cores, mini-cores, and chips) using a KLY-3 Kappabridge (AGICO). To ensure that the specimens were statistically anisotropic with 95% confidence, only samples with F-tests for anisotropy >5 were selected for further analyses (Hext, 1963). These were analysed using the ANISOFT 4.2 software (Chadima and Jelínek, 2008) which computes the susceptibility tensor in the form of an ellipsoid. The three principal susceptibility axes of the ellipsoid are represented as $K_1 > K_2 > K_3$. Each specimen was weighed to calculate the mass susceptibility (χ_m) for data comparison, and these measurements were used to calculate:

1. Mean susceptibility, $K_m = (K_1 + K_2 + K_3)/3$ (Nagata, 1961);
2. Degree of magnetic anisotropy, $P' = \exp.\{2[(\ln K_1 - \ln K_m)^2 + (\ln K_2 - \ln K_m)^2 + (\ln K_3 - \ln K_m)^2]\}^{1/2}$ (Jelinek, 1981);
3. Shape parameter, T = [{2ln(k2/k3)}/ln(k1/k3)] - 1, where Value of T varies from +1 for oblate to −1 for prolate fabric (Jelinek, 1981);
4. Magnetic lineation, $L = K_1/K_2$ (Balsley and Buddington, 1960);
5. Magnetic foliation, $F = K_2/K_3$ (Stacey et al., 1960).

Next, we performed the palaeomagnetic measurements to check the coevality of dyke emplacement. We measured natural remanent magnetization (NRM) of each specimen using a JR6 spinner magnetometer. Sister pilot specimens were stepwise demagnetized using alternated field (AF), field from 5 mT up to 120 mT, and thermal demagnetization, up to a temperature of 580 – –600 °C. Alternating field demagnetization provided stable and well-defined data, so all specimens were demagnetized to isolate the characteristic remanent magnetisation (ChRM) using the AF demagnetization method. Results were processed using the Remasoft 3.0 software (Chadima and Hrouda, 2006).

Finally, rock magnetic measurements were carried out on representative cores to characterise the different magnetic phases, and to better understand their contribution to both remanence and magnetic fabric. Two samples from each dyke, taken from the dyke centre and dyke boundary, were subjected to isothermal remanent magnetization (IRM) acquisition by systematically increasing the applied field up to 1.2 T. Coercivity of remanence (B_{cr}) was then extrapolated by measuring the back-field curves and the mean remanence coercivity (Bh), and the

Table 1
Mean AMS data of Mount Calanna dykes.

Dyke	Samples	n/N	χ_m	st. dev.	L	F	P′	T	K_1				K_2				K_3			
			(x 10^{-3} m^3 kg^{-1})						D	I	E_{1-2} (°)	E_{1-3} (°)	D	I	E_{1-3} (°)	E_{1-2} (°)	D	I	E_{3-2} (°)	E_{3-1} (°)
CD1	CD1–1	7/8	12.89	0.79	1.010	1.023	1.040	0.266	57	24	10.8	6.6	327	4	10.9	5.1	229	66	7.6	4.0
	CD1–4	13/13	12.54	1.92	1.050	1.013	1.070	−0.526	193	24	6.4	4.0	89	28	17.7	5.9	317	52	17.7	4.7
	CD1–2	7/11	14.69	2.30	1.030	1.011	1.040	−0.362	23	4	17.8	3.6	115	26	20.6	14.8	286	64	19.0	4.0
	CD1–3	7/7	18.06	1.35	1.020	1.012	1.070	−0.318	6	4	8.7	5.6	100	43	10.3	7.2	271	47	9.5	6.3
CD2	CD2–2	6/6	27.79	1.77	1.021	1.010	1.033	−0.307	200	45	17.1	9.7	69	33	21.7	12.6	320	27	20.9	6.7
	CD2–3	9/9	20.50	7.74	1.018	1.022	1.041	0.093	196	47	9.3	3.8	81	22	9.3	7.8	335	35	7.9	3.9
	CD2–4	7/9	25.39	1.02	1.027	1.018	1.046	−0.128	118	24	47.7	16.8	224	30	48.5	10.0	356	50	26.0	10.4
	CD3–2	11/13	15.13	1.36	1.013	1.022	1.036	0.294	1	46	11.4	6.6	238	28	13.7	8.8	129	31	11.8	6.7
	CD3–3	11/15	19.41	1.20	1.016	1.018	1.035	0.081	134	53	17.7	5.8	236	9	20.8	12.4	332	35	16.8	5.8
	CD3–4	9/13	13.95	1.90	1.016	1.014	1.031	0.000	269	60	25.8	15.0	97	29	35.7	20.0	5	4	36.3	10.7
	CD3–5	10/13	15.17	1.55	1.016	1.012	1.029	−0.146	222	70	28.5	12.5	117	5	28.9	23.2	25	19	25.3	12.0
CD4	CD4–1	7/9	13.90	0.53	1.011	1.004	1.016	−0.480	53	22	15.3	2.3	271	63	51.6	14.8	149	15	51.5	2.6
	CD4–2	2/2	11.55	0.25	1.026	1.011	1.039	−0.392	102	16	–	–	7	16	–	–	234	68	–	–
	CD4–3	7/7	11.99	0.89	1.010	1.009	1.019	−0.049	230	36	16.8	5.8	106	38	15.6	6.9	346	32	9.7	5.8
	CD4–4	3/3	17.61	0.88	1.006	1.007	1.013	0.178	115	8	–	–	349	77	–	–	206	11	–	–
CD5	CD5–1	4/4	19.24	0.92	1.012	1.028	1.041	0.394	125	1	–	–	215	25	–	–	32	65	–	–
	CD5–2	7/7	12.89	1.22	1.012	1.026	1.039	0.361	116	2	8.0	6.0	208	29	8.0	3.5	23	61	6.3	2.9
	CD5–3	12/12	14.57	1.36	1.016	1.026	1.044	0.233	117	13	6.8	1.5	210	12	7.2	4.8	341	73	5.4	1.4
	CD5–4	18/18	18.00	2.34	1.021	1.024	1.046	0.067	288	12	11.7	7.9	191	29	18.5	6.7	38	59	16.5	8.9
	CD5–5	17/19	17.61	1.54	1.026	1.012	1.039	−0.367	161	26	14.6	4.6	260	19	15.9	11.2	22	57	12.9	4.6
CD6	CD6–1	2/2	17.24	0.62	1.005	1.005	1.010	0.063	59	50	–	–	295	25	–	–	190	29	–	–
	CD6–2	5/6	22.58	0.65	1.013	1.014	1.028	−0.032	6	63	13.8	8.0	179	27	47.2	9.4	270	3	46.8	8.0
	CD6–4	12/15	19.24	5.95	1.012	1.017	1.031	0.064	307	36	31.4	14.0	200	23	32.7	13.1	84	45	18.7	12.0
CD7	CD7–1	6/6	14.00	0.89	1.009	1.021	1.031	0.445	246	61	28.0	8.2	151	3	27.3	7.9	60	29	12.5	5.3
	CD7–2	6/6	13.54	0.79	1.007	1.026	1.035	0.595	208	42	63.0	12.0	319	22	62.4	5.6	68	40	26.3	7.7
	CD7–3	5/6	9.91	6.62	1.010	1.030	1.042	0.514	181	68	12.2	1.7	275	2	17.3	4.1	6	22	13.4	1.8
CD8	CD8–1	10/12	14.39	0.56	1.012	1.020	1.033	0.172	134	42	20.0	7.0	304	48	19.8	2.2	40	5	7.2	2.2
	CD8–2	6/7	17.06	0.75	1.010	1.022	1.032	0.419	147	30	17.6	3.6	256	29	18.0	8.2	20	45	9.4	4.0
CD9	CD9–2	2/2	17.99	0.05	1.029	1.033	1.063	1.073	257	21	–	–	158	23	–	–	26	58	–	–
	CD9–2	19/20	18.65	1.08	1.033	1.033	1.068	0.050	177	26	19.1	2.9	294	43	19.6	12.3	66	36	13.2	2.9
CD10	CD10–1	14/14	13.41	0.34	1.015	1.021	1.037	0.166	314	5	6.8	1.8	221	31	10.7	6.3	52	59	10.7	2.7
	CD10–2	5/6	18.04	0.76	1.008	1.023	1.033	0.448	166	11	26.2	5.7	270	53	27.4	11.2	68	35	14.8	4.9
	CD10–3	5/5	17.62	0.55	1.018	1.021	1.040	0.092	169	34	16.4	7.6	78	2	17.9	8.5	346	56	12.6	5.5

n = Number of specimens considered; N = number of specimens measured; χ_m = mass susceptibility; L = magnetic lineation; F = magnetic foliation; P′ = corrected degree of magnetic anisotropy; T = shape parameter; D = declination; I = Inclination; E = confidence limit; K_1 = maximum susceptibility axis; K_2 = intermediate susceptibility axis; K_3 = minimum susceptibility axis

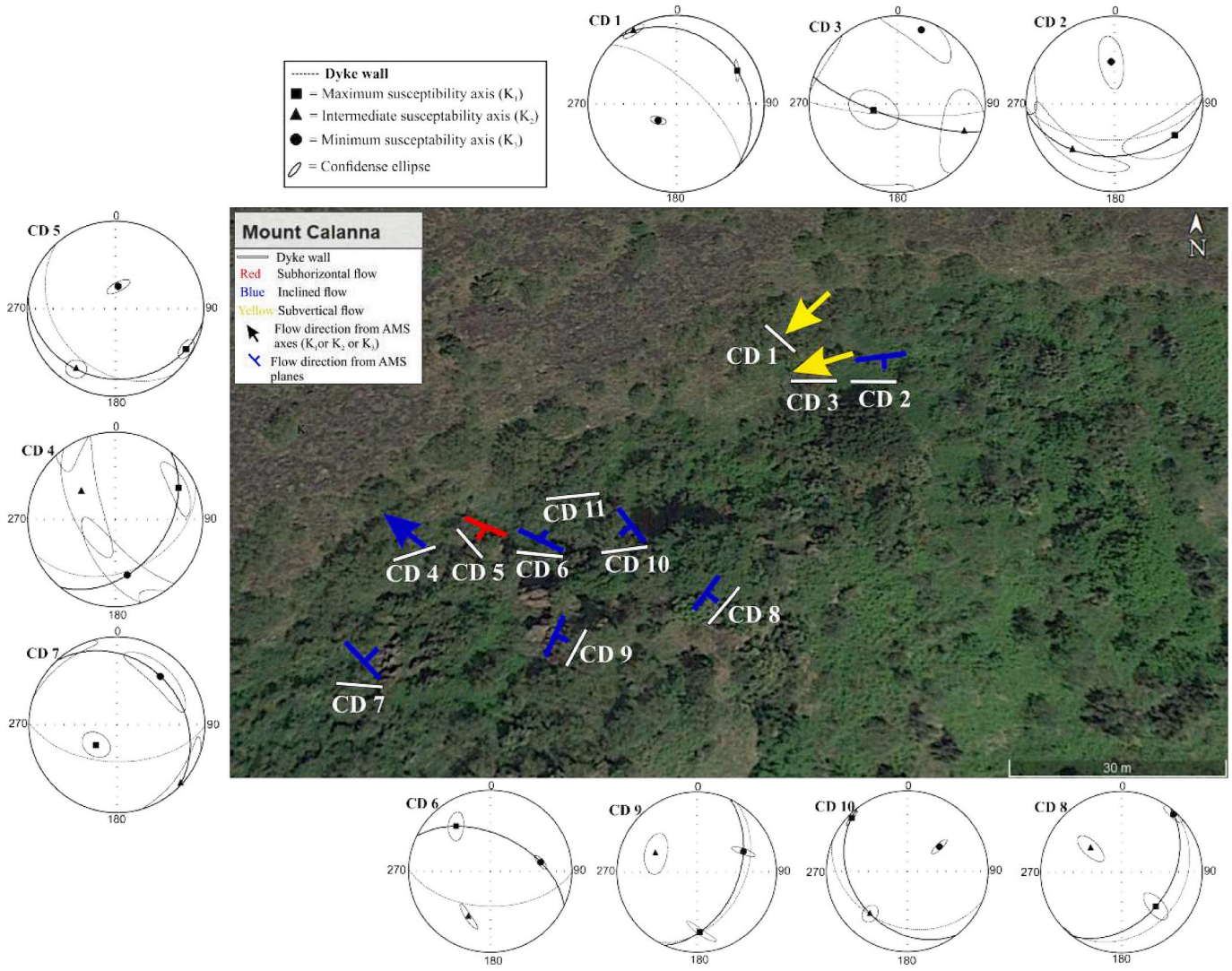

Fig. 10. Google Earth image of northern part of Mount Calanna with the location and orientation of sampled dykes (white line) along with the inferred flow direction by magnetic fabrics. Stereonets depict the orientation of the three susceptibility axes with their relative confidence ellipsoid and the magnetic plane considered to define the flow direction using the proposed practise along with the dyke boundaries.

dispersion parameter (DP) was obtained using MAX UnMix (Maxbauer et al., 2016). Moreover, we performed the thermal demagnetization on the three IRM components (Lowrie, 1990) on one representative specimen from each sample to find the unblocking temperature of each component. To do this, we applied a field of 1.0, 0.6, and 0.1 T, along the x-, y-, and z-axis of the samples, respectively. Finally, specimens were subjected to progressive thermal demagnetization up to 550–600 °C, where the susceptibility values were recorded after every phase to identify thermally modified mineralogical alterations.

3.2. Petrofabric and image analysis

Thin sections were prepared to obtain the mineral assemblage, texture, and shape preferred orientation (SPO) of the silicate fabrics. Two oriented specimens from each dyke were selected: one from the dyke centre and one from the dyke boundary, and thin sections were prepared along the K_1-K_2, K_2-K_3, and K_1-K_3 planes for specimens having normal, inverse, and intermediate fabrics, respectively. High spatial resolution images from each thin section were captured using an Olympus B × 4 optical microscope. Oriented micrographs were transformed into grayscale, and the plagioclase lath distribution was assessed using ImageJ (Rasband, 2012). Because ferromagnetic minerals crystallise at a late stage in cooling process, and after magma flow has ceased (Geoffroy et al., 2002; Das and Mallik, 2020), we compared the shape preferred orientation of the silicates with the AMS fabric.

3.3. Geochemical analysis

Whole rock geochemistry analysis was completed for all nine unaltered samples. Samples were crushed using a hydraulic press fitted with high purity steel plates, and only chips with minimal surface alteration and which were free of vesicles were selected for further analyses. Analyses were carried out on rock powder pulverized using a Spex® ball mill fitted with an alumina vessel. Major element analysis was conducted at the Hamilton Analytical laboratory (New York, USA) using a Thermo ARL Perform'X Spectrometer. Loss on ignition (LOI) was measured by heating the samples overnight at 900 °C. REE, HFSE, LFSE and transition metals were obtained for the same samples using the Agilent 8900 ICP-MS QQQ at the Department of Geology and Geological Engineering of the Colorado School of Mines (Colorado, USA). The standard reference material, BHVO-2 and an unknown were run to check the precession of data (Jochum et al., 2016). Filtering of results affected by alteration was made on the basis of Loss on Ignition (LOI) values, where only whole rock analyses having LOI < 3 wt% were considered

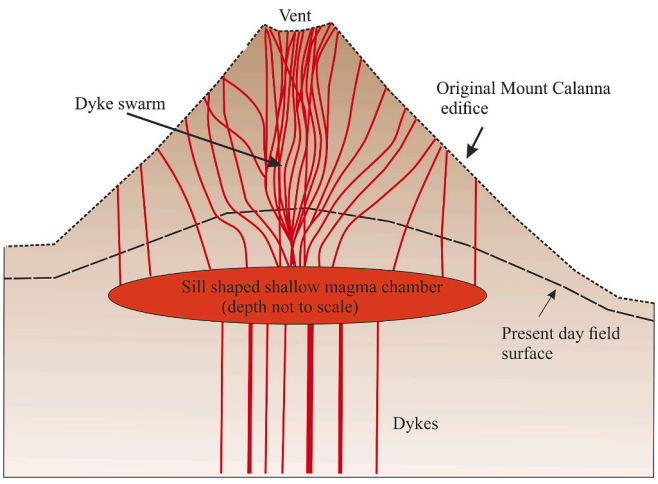

Fig. 11. Simplified schematic illustrations of the Mount Calanna plumbing system, with a deep network of dikes and sills that eventually join near the summit vent of Mount Calanna. What we see now is the shallow part of the plumbing system, where dykes make up at least 40% of the total volume (Ferlito and Nicotra, 2010).

(Table 2). This reduced the number of dykes that could be considered as fresh (unaltered) to six (Table 2).

4. Results

The dykes of Mount Calanna are 0.5–3 m thick and are dissected by two sets of joints, a NW-SE sub-vertical set and a sub-horizontal NE-SW oriented set (Fig. 1e). Based on our field observations and structural data, we thus classify the sampled dykes as follows:

1) Those emplaced sub-vertically and located in the lower part of Mount Calanna (CD1, CD2, and CD3);
2) Those emplaced sub-horizontally and located in the upper part of Mount Calanna (CD4 – CD11).

4.1. AMS and new approach to infer magma flow in dykes

Among the sampled dykes mass susceptibility (χ_m) does not change significantly between the sub-vertical and sub-horizontal groups. For sub-vertical dykes, χ_m varies between 1.25 and 2.78 $\times$ 10^{-2} m^3kg^{-1}, with an average of 1.80 $\pm$ 0.49 $\times$ 10^{-2} m^3kg^{-1} (Fig. 2a), and for sub-horizontal dykes between 0.99 $\times$ 10^2 and 2.26 $\times$ 10^{-2} with an average of 1.60 $\pm$ 0.31 $\times$ 10^{-2} m^3kg^{-1}. Dyke CD2 shows a slight positive deviation from the rest of the dykes, and CD11 has lower values (mean χ_m of 1.48 $\times$ 10^{-3} m^3kg^{-1}) suggesting different magnetic mineral assemblages for these two cases.

The shape parameter varies from oblate to prolate in both groups (Fig. 2b). Corrected degree of magnetic anisotropy is relatively low, ranging from 1.013 to 1.070 with an average of 1.040 (Fig. 2c). No clear correlation was found between degree of magnetic anisotropy, the shape factor, and dyke type (sub-vertical or sub-horizontal). Within the same dyke, it is common to have both oblate and prolate fabrics (Fig. 2b). In some dykes this distribution changes systematically across the dyke. For example, in CD5 the shape of the AMS ellipsoid is prolate at the dyke centre, but oblate at the dyke edges (Fig. 2d). Ten dykes gave well-constrained AMS data, but CD11 gave highly dispersed data due to high degrees of alteration. Low values of χ_m confirm alteration-induced hematite formation in CD11 (see Supplement 2). Hence, CD11 was excluded from further magnetic fabric interpretation. The final AMS results are given in Table.

The three principal susceptibility axes are generally well-clustered (Fig. 3), but their distribution changes with dyke thickness, changing between dyke centre and edge in each case. Magnetic fabric shows distinct patterns depending on the dyke type (sub-vertical/horizontal). For example:

1. In sub-vertical dyke CD3, at the dyke centre mean K_1 axes are inclined to sub-horizontal and oriented at a high angle with respect to the dyke wall (Fig. 3b). Instead, near the dyke boundary, the K_1 axis is sub-vertical and aligns with the orientation of the dyke wall (Fig. 3a).
2. CD2 shows well-clustered AMS axis distributions at the dyke centre (Fig. 3d), whereas it is less constrained at the dyke boundary (Fig. 3c). Moreover, the foliation plane of CD2 is parallel/subparallel to the dyke wall at both the dyke centre and boundary.
3. For sub-horizontal dyke CD10, at the dyke boundary the K_1 axes plunge towards the NW (Fig. 3e), while at the dyke centre K_1 plunges towards the South (Fig. 3f).
4. Dyke CD8 has a distinct vertical foliation plane near the dyke boundary (Fig. 3 g) and an inclined foliation plane at dyke centre (Fig. 3 h).

In both groups of dykes, the intermediate susceptibility axis has a larger confidence ellipsoid with a high value of confidence angles in comparison to the K_1 and K_3 axis.

Considering the evolution of AMS data interpretation over the last few decades, we use our data to propose a framework for inferring flow direction in dykes from AMS data (Fig. 4). Based on the orientation of the three susceptibility axes with respect to that of the dyke wall, we grouped the samples into four classes following the classification of Wiegand et al. (2017):

1. *Normal Fabrics*: K_1 and K_2 sub-parallel to the dyke wall, and K_3 is perpendicular to the dyke plane (Fig. 4a-i);
2. *Intermediate Fabrics*: K_1 and K_3 axes subparallel to the dyke plane, with the K_2 axes perpendicular to the dyke plane (Fig. 4a-ii);
3. *Inverse Fabrics*: K_1 axis normal to the dyke plane, with the K_2 - K_3 plane parallel to dyke plane (Fig. 4a-iii);
4. *Oblique Fabrics*: any magnetic fabrics with variable orientations in terms of magnetic foliation and lineation, and with significant discrepancy in respect to the dyke plane and which cannot be accommodated in any of the three classes (Fig. 4a-iv).

In all cases, a deflection of 35^0 to the dyke plane is accepted (Raposo and Ernesto, 1995; Wiegand et al., 2017). Within these classes we use the shape of the susceptibility ellipsoid, whether prolate or oblate, to infer flow direction (Fig. 4b).

4.2. Palaeomagnetism

The NRM value is in the range 0.9–30 Am^{-1}. Because the thermal demagnetisation did not give stable results, we used only AF data for interpretation (Fig. 5). Most of the samples were completely demagnetized within 60–100 mT, and the Median Destructive Field (MDF) ranges from 10 to 20 mT. Zijderveld diagrams confirm the presence of two magnetization components, with a well-defined ChRM that trends towards the origin and a secondary low-coercivity component of possible viscous origin. This behaviour of the magnetization vector is the most common, but for some dykes, the remanent magnetization clearly shows a decrease in inclination during demagnetization (e.g., sample CD5–4 CE in Fig. 5a).

Using principal component analysis, we calculated the ChRM, choosing a maximum angular deviation of $<6^\circ$ (Fig. 6). We applied Fisher's Statistics (Fisher, 1953) to compute the mean ChRM at the site level (Table S1–1, Supplement 1). The directional result for each dyke is plotted in Fig. 5. We obtained two clusters for the ChRM directions, one with declination (D) = 352.0°; inclination (I) = 65.0°; precision

Table 2
Major element on anhydrous basis (wt%) and trace element (ppm) data for the dykes of Mount Calanna.

	CD-1	CD-2	CD-3	CD-5	CD-6	CD-7	CD-8	CD-9	CD-10
SiO2	51.27	49.64	52.07	54.53	51.24	54.70	51.33	50.81	55.12
TiO2	1.85	2.00	1.78	1.53	1.67	2.06	1.73	1.73	1.39
Al2O3	19.57	18.36	19.47	19.66	19.27	20.51	19.27	18.98	19.94
$FeO_{(tot)}$	7.90	9.23	7.57	6.38	8.28	6.46	8.14	8.30	6.44
MnO	0.15	0.18	0.15	0.13	0.16	0.06	0.17	0.17	0.11
MgO	3.26	3.50	2.18	2.66	3.64	4.25	2.61	3.11	2.36
CaO	8.10	9.22	8.81	7.23	7.59	4.63	8.77	8.71	6.86
Na2O	5.04	4.77	4.73	4.82	5.73	4.55	4.87	5.09	4.87
K2O	1.93	2.08	2.25	2.25	1.75	2.01	2.18	2.14	2.32
P2O5	0.93	1.01	0.98	0.80	0.68	0.77	0.93	0.96	0.59
LOI (%)	2.57	0.64	1.38	2.88	3.63	4.69	1.13	0.44	2.25
Ag	0.050	0.055	0.045	0.058	0.058	0.022	0.061	0.050	0.042
As	1.12	2.24	1.50	1.17	1.26	0.88	1.74	1.62	1.61
Ba	598	821	784	780	757	662	733	710	810
Bi	0.034	0.059	0.066	0.052	0.043	0.056	0.062	0.054	0.060
Cd	0.06	0.09	0.12	0.15	0.09	0.07	0.10	0.07	0.10
Cr	7.4	7.6	5.3	8.4	8.0	4.4	4.8	10.7	6.2
Cs	0.9	0.8	1.3	0.9	1.1	0.6	1.2	1.2	0.9
Cu	54.51	58.89	63.12	48.72	42.06	40.13	60.22	59.41	46.13
Ga	22.45	23.80	23.38	23.52	22.18	24.05	23.15	23.17	24.24
Ge	1.59	1.91	1.81	1.97	1.79	2.05	1.89	1.70	1.85
Hf	4.58	4.99	5.30	5.29	4.72	4.78	5.12	5.16	5.61
Mo	2.5	5.2	2.0	2.3	2.4	2.9	3.7	3.6	2.6
Nb	57.58	81.46	77.12	75.61	76.41	68.83	75.62	74.89	77.76
Ni	8.2	10.1	12.5	12.0	10.2	6.7	5.7	8.2	5.5
Pb	6.17	7.86	8.60	8.64	6.58	3.85	8.61	8.30	9.17
Rb	43.20	40.95	51.12	49.80	47.91	36.27	47.99	47.76	48.83
Sb	5.19	5.26	5.31	5.13	5.00	5.37	5.30	5.28	5.30
Sc	12	15	14	9	12	15	13	13	8
Sn	1.77	1.89	1.87	1.80	1.58	1.75	1.80	1.81	1.84
Sr	1046.54	1357.99	1355.14	1215.85	1075.36	996.64	1317.22	1287.62	1324.74
Ta	2.86	3.93	3.86	3.68	3.64	3.31	3.78	3.79	3.78
Th	7.57	12.19	9.98	11.18	10.20	9.49	9.78	9.62	10.87
U	2.47	3.76	3.17	3.50	3.22	3.11	3.13	3.10	3.57
V	141	202	169	127	174	173	159	165	107
Y	26.63	28.54	30.86	41.10	29.60	22.29	25.86	25.49	25.75
Zn	86.19	101.57	98.29	185.47	100.12	129.55	86.98	87.17	103.45
Zr	207.86	232.51	245.03	250.80	229.19	211.04	234.87	238.25	264.73
La	53.65	82.27	72.35	86.01	74.35	55.93	68.98	67.82	74.11
Ce	109.00	154.21	142.69	165.37	138.95	111.91	135.99	135.69	135.86
Pr	12.11	17.01	15.98	18.62	15.12	12.13	15.19	15.12	14.62
Nd	46.16	63.54	60.42	68.33	56.02	44.74	57.42	56.53	53.53
Sm	8.55	10.88	10.47	12.03	9.68	7.74	9.66	9.79	8.80
Eu	2.71	3.20	3.14	3.54	2.89	2.39	2.94	2.89	2.69
Gd	6.95	8.44	8.34	10.25	7.89	5.59	7.51	7.46	6.79
Tb	1.02	1.14	1.17	1.45	1.09	0.83	1.06	1.02	0.95
Dy	5.21	5.66	5.88	7.66	5.58	4.45	5.23	5.03	4.79
Ho	0.94	1.04	1.06	1.43	1.00	0.82	0.95	0.93	0.91
Er	2.390	2.566	2.676	3.659	2.608	2.164	2.380	2.321	2.362
Tm	0.33	0.34	0.37	0.50	0.36	0.30	0.33	0.33	0.34
Yb	2.086	2.014	2.254	2.949	2.192	2.049	1.878	1.923	2.151
Lu	0.311	0.290	0.328	0.445	0.306	0.305	0.299	0.285	0.333

parameter (k) = 27; and α_{95} confidence cone = 3.4°, and a second cluster shared by three dykes with D = 27.0°, *I* = 31.0°, k = 17 and α_{95} = 6.8°. The two clusters are independent of the mode of emplacement (sub-vertical and sub-horizontal).

4.3. Rock magnetism

All samples yielded an IRM curve with a saturation of magnetization being attained around 100–200 mT, indicating a low coercivity component. The mean remanence coercivity (Bh) and dispersion parameter (DP), after unmixing the IRM curve, does not show any significant change between the two groups (Fig. S2–2, Supplement 2). Irrespective of dyke position and mode of injection, most of the dykes confirm the presence of three components (Fig. 7a):

1. a low-coercivity component, where the relative contribution varies between 8% and 86%,
2. an intermediate-coercivity component, where the relative contribution varies between 23% and 98%, and
3. a high-coercivity component, where the relative contribution ranges between 2% and 14%.

The only exception is shown by CD11 (Fig. S2–2, Supplement 2)., which shows the dominance of a high-coercivity component (49%).

Thermal demagnetization of the three IRM components showed the same behaviour with the dominance of a soft fraction (<0.1 T) (Fig. 7b). The medium component is usually weak, while the hard component is negligible. In most samples, >95% of the remanent magnetization was removed at around 350–400 °C (Fig. S2–1, Supplement 2). For the rest, unblocking temperatures progressively dropped to a maximum of 550–600 °C, suggesting a range of Ti-content. The initial decline of magnetization around 350 °C suggests the presence of soft magnetic carriers such as iron sulphides or Ti-rich titanomagnetite (Weaver et al., 2002). Even though the three IRM components have the same thermal demagnetization trend in all dykes, the contribution of the intermediate

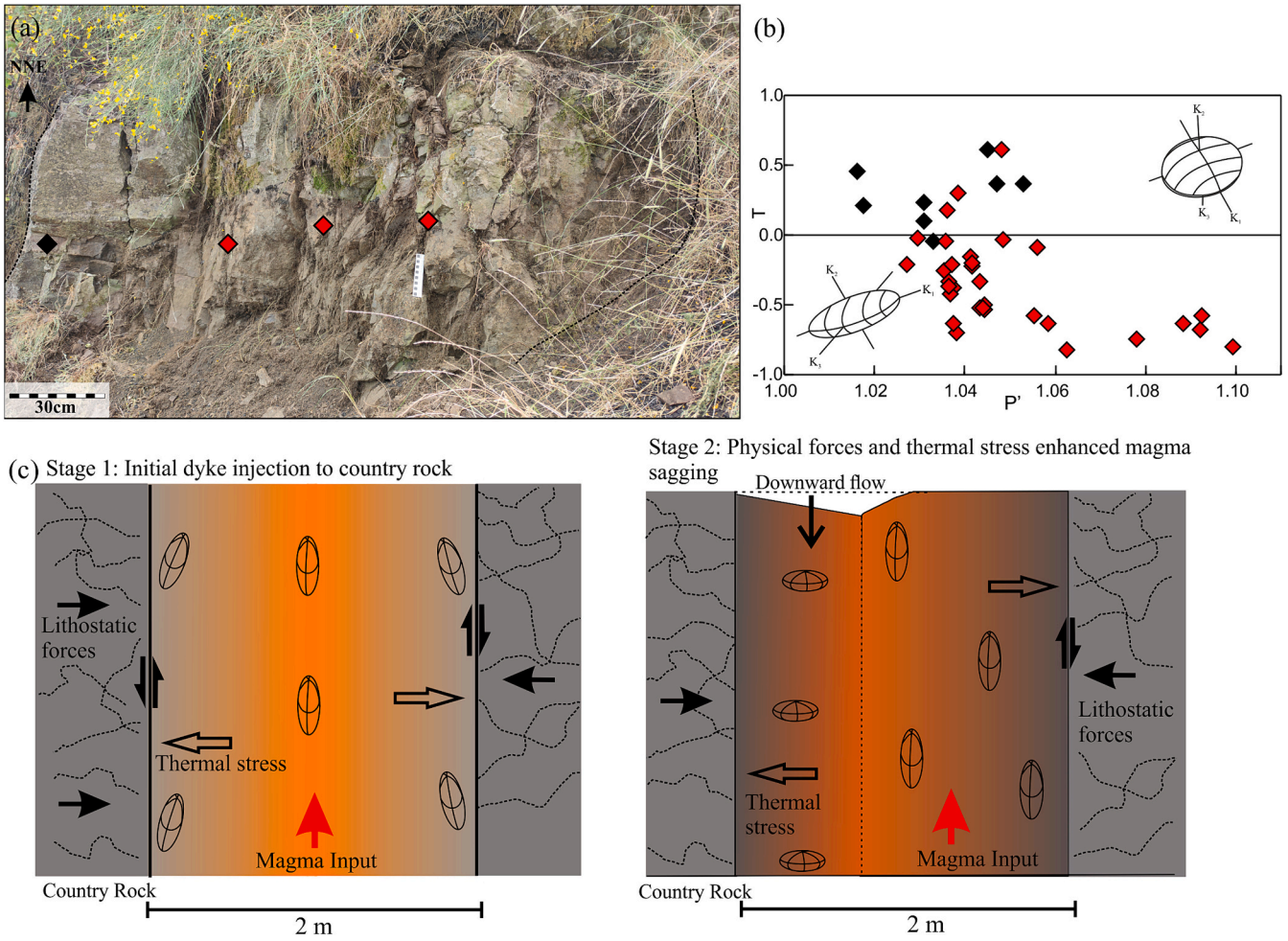

Fig. 12. (a) Field photo of CD1 (a sub-vertically emplaced dyke) with sampling sites. (b) Distribution of magnetic fabrics ellipsoids along dyke width. The black and red diamonds show oblate and prolate ellipsoid respectively (c) Model of *syn*-and post-emplacement mechanism of dykes. As the magma starts cooling down, the lithostatic forces along with thermal stress increase, resulting in slight bending along a weak plane and sagging of the downward bent part. This sagging and downward flow overprints the primary prolate fabrics along the NNE boundary to leave oblate fabrics.

and hard components varies among specimens (Fig. 7b).

4.4. Petro-fabric and image analysis

All dykes exhibit a porphyritic texture with plagioclase and clinopyroxene phenocrysts, with minor olivine and opaque oxides (Fig. 8). The groundmass has a hyalopilitic texture with plagioclase microlites, along with altered brown glass. Modal analyses yield 1 to 5% of opaque magnetic grains. Phenocrysts are euhedral to subhedral, with sizes varying from 1 to 4 mm. Based on microscopic analyses, CD6 and CD7 are mostly altered, with vesicles filled with reddish-brown secondary minerals (Fig. 8e). Although the rest of the dykes do not show significant alteration, phenocrysts are highly fractured in most cases, especially in samples collected along the dyke boundaries.

Fig. 8 shows the comparison of silicate fabric to AMS fabric for three representative dykes, a sub-vertical dyke (CD2), and two sub-horizontal dykes (CD6 and CD8). Seven dykes have samples collected near the dyke wall that display good consistency between petrofabrics and magnetic fabrics. Instead, for the dyke centre, in most cases, different crystal species show distinct preferred orientations. In CD2, the silicate and AMS fabrics show a consistent orientation, which is that of the NNW-SSE direction for dyke boundary (Fig. 8a). However, at the dyke centre samples show two flow orientations for silicate fabrics (WNW-ESE and WSW-ENE), but a single ENE-WSW direction for magnetic fabrics. (Fig. 8b). In CD8, we obtain a small secondary maximum in the NE-SW direction for silicate fabrics for the dyke boundary sample, the primary maximum is oriented in the same direction as that of AMS fabric (Fig. 8c). However, the dyke centre sample does not show a consistent orientation for plagioclase laths and opaque magnetic minerals inferred from AMS (Fig. 8d). Similarly, for CD6, the sample from the dyke boundary has plagioclase laths oriented in the same direction as that of opaque minerals (Fig. 8e), while for the sample from dyke centre silicate fabrics and AMS fabrics display different orientations (Fig. 8f).

4.5. Whole rock geochemistry

Whole rock major elements mainly plot in the mugearitic field of the Total Alkali Silica (TAS) diagram (Le Maitre et al., 2002; Fig. 9a). Mount Calanna dykes are typically characterised by SiO_2 of 48.8–50.7 wt%, and high values of TiO_2 (1.590–1.966 wt%) and MgO (8.1–10.6 wt% MgO) (Table 1). This confirms that the dykes of Mount Calanna have the same composition of the Na-alkaline suite of Etnean succession (cf. Cristofolini et al., 1991).

In the TAS diagram, our data mostly plot within the field of Ancient Alkaline Centres (AAC), with an overlap on the most basic region of Trifoglietto compositions (Fig. 9a). When major elements of our dyke samples are plotted together with Ancient Alkaline Centre compositions, they follow within the compositional field of the Ancient Alkaline centre eruptive phase (Figs. 9b-c) and supporting the findings of Ferlito and Nicotra (2010). Thus, the dykes studied may be the feeder dykes

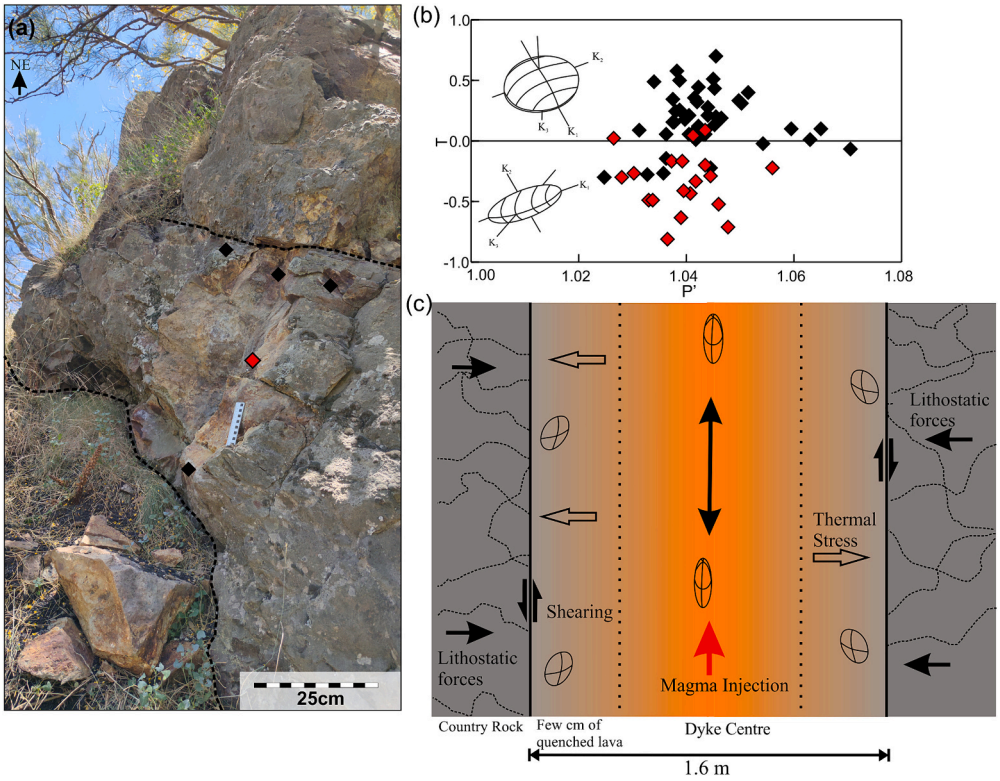

Fig. 13. (a) Field photo of CD5 (sub-horizontally emplaced dyke) with sampling location. (b) Distribution of magnetic fabrics ellipsoids along dyke width. (c) Schematic representation of the magma propagation along the dyke. Near dyke boundary, the few cm of quenched lava had an inward cooling trend and thereby formed oblate. Whereas in the dyke centre, where magma remains active for weeks, even months to years, magma has a lateral flow direction, either in an upward or downward direction.

associated with the actual lava flows in the successions. In terms of trace element distribution, all dykes, regardless of injection mode, show a similar distribution pattern, confirming all dykes are having the same parent magma (Fig. 9d).

5. Discussion

5.1. Inferred magma flow direction in dykes

Discussion among rock magnetists has focused on to how to interpret magma flow direction in dykes using AMS (e.g., Geoffroy et al., 2002; Callot and Guichet, 2003; Cañón-Tapia, 2004). Khan (1962) was one of the first to use AMS to infer flow fabrics in igneous rocks, using the K_2 axis as a proxy for flow directions in dykes. Later, Wing-Fatt and Stacey (1966) proposed that the maximum susceptibility axis (K_1) is a more precise proxy for flow direction. However, using image analysis of silicate fabrics along with magnetic fabrics in Tertiary basaltic dykes from Greenland, Geoffroy et al. (2002) showed the limitations of using the K_1 axis to represent flow direction. Instead, Geoffroy et al. (2002) proposed that the magnetic foliation plane (K_1–K_2) more precisely defined flow direction in dykes. The most common criteria used to interpret flow direction is the magnetic lineation (K_1) in the case of prolate fabrics, and the magnetic foliation plane for oblate fabrics (Delcamp et al., 2015; Andersson et al., 2016; Schmiedel et al., 2021). Domain structure, along with the orientation of the susceptibility axis with respect to the dyke wall (Hrouda, 1982; Rochette et al., 1992; Das et al., 2021) and the imbrication of the foliation plane at the dyke wall (Knight and Walker, 1988; Das et al., 2021) have also been used to infer flow directions. However, there remains no well-established practise for the study of flow direction in dykes using AMS. So, the approach adopted here can provide a new framework for constraining the flow direction in dykes from AMS data.

To validate our approach, we checked the consistency of the magnetic flow fabric with the orientation of the plagioclase laths obtained from thin section analysis. The consistency of flow direction at dyke boundary obtained from both methods, where rapid cooling of magma at the dyke wall freezes in the initial flow direction, confirms the reliability of the approach (Fig. 8). Instead, the random orientation of plagioclase laths at the dyke centre is likely due to the lateral flow, as well as back flow and convection, at dyke centre, as it can remain fluid for days or weeks after emplacement and after eruptive flow has ceased. We can rule out the possibility of reworking and collapse of the three-dimensional plagioclase network, as pointed out by Philpotts and Dickson (2000), as our dykes are small, where the maximum dyke thickness was 3 m, and cooled relatively quickly.

The flow directions for each dyke, as obtained from the dyke boundary samples, are given in Fig. 10 along with the representative equiareal projections. The AMS results show more than one flow direction, with sub-horizontal, inclined, and sub-vertical distributions, indicating the complexity of the emplacement process. The structural data of Ferlito and Nicotra, 2010 agree with this classification of the Mount Calanna dykes (Fig. S3–1, Supplement 3) showing, broadly, two classes of dyke in terms of orientation and flow direction.

Flow direction is consistently NE-SW in the case of the sub-vertically emplaced dykes, but NE-SW and NW-SE for sub-horizontal dykes (Fig. 10). We also find that dykes towards the top of Mount Calanna have an inclined to sub-horizontal flow direction. The lateral migration of the feeder dyke from the upper part of central conduit to the surface may be reflected in horizontal magma flow direction towards the top of Mount Calanna. The elevated tensile stress exerted at the upper section of the conduit, close to the volcanic edifice along with the neutral buoyancy may cause the lateral propagation of magma (Geshi, 2008; Pinel et al., 2017). Indeed, regional stress field also plays an important role in the lateral migration of magma (Gautneb and Gudmundsson, 1992;

Maccaferri et al., 2011; Bagnardi et al., 2013; Pinel et al., 2017). But the homogeneous characteristics of sub-vertical and sub-horizontal dykes indicate that they were likely emplaced under same regional stress field. This kind of dyke propagation from the central conduit has already been observed at Mount Etna (Aloisi et al., 2009) and other sites including Stromboli (Acocella et al., 2006a), Hawaii (Decker, 1987) and Vesuvius (Acocella et al., 2006b). In contrast, in the lower part of the Mount Calanna structure, we find sub-vertical to inclined flow directions. Considering the geometry of the Mt. Calanna plumbing systems proposed by Ferlito and Nicotra (2010), where the subvolcanic structure is fed by the shallow sill-shaped magma reservoir connected to a deep magma chamber, the subvertical magma flow may be due to direct emplacement of the dyke from the magma reservoir (Fig. 11). Since the major and trace element data show no difference among the two groups of dykes, we can rule out the possibility of direct propagation from the deep seated main magma chamber for the sub-vertical dykes, as in the case of the radial dyke swarm in Komochi volcano (Geshi, 2008) and the present summit vent of Mount Etna (Aloisi et al., 2009). Given the subvolcanic model of Mount Calanna proposed by Ferlito and Nicotra (2010), wherein a deep magma chamber is connected to a shallow sill-like reservoir, it is likely that subvertical dykes could be injected directly from this shallow reservoir due to increased magma pressure. The dyke evolution and plumbing system identified at Mount Calanna is similar to the model proposed by Geshi (2008) for the 'lateral' and 'vertical' types of dyke emplacement at Komochi volcano.

5.2. Magmatic and evolutional setting of Mount Calanna in the framework of Etna's evolution

Previous studies have identified the presence of a few fresh "unaltered dykes" belonging to the Mongibello volcanic phase at Mount Calanna (Ferrari et al., 1989; Ferlito and Nicotra, 2010). Clustering of the ChRM direction, and its conformity with the geocentric axial dipole direction of the primary cluster (Fig. 6) along with the coherent characteristics of major and trace elements (Fig. 9), confirms that all dykes considered here were erupted in the same epoch. Given that the three dykes that make up the secondary cluster, CD11, CD6 and CD9, lie along a plane with shallow ChRM inclinations and that Mount Calanna is mostly dissected by faults (Ferlito and Nicotra, 2010), the formation of the secondary cluster can be attributed to fault reworking. The Mount Calanna dyke swarm thus resulted from single and/or multiple intrusion events and associated eruptions, that occurred over a short period of time.

The major element composition, especially the high percentages of TiO_2 and P_2O_5, confirm that the Mount Calanna dykes belong to Etna's Ancient Alkaline Centre phase (Table 2) (Cristofolini et al., 1991; Ferlito and Nicotra, 2010). Even though the sub-horizontal and sub-vertical dykes emplaced from the central conduit and shallow sill-like magma chamber respectively, major element and trace element do not show any change in the magma maturity. This is due to the fact that the magma did not stay in the shallow system for sufficient time to undergo fractional crystallization.

The dyke swarm observed in Mount Calanna is associated with the N-S direction of the maximum extensional stress field (Ferlito and Nicotra, 2010). Mount Etna's present regional tectonic setting, characterised by NNW-SSE and NE-SW orientations and the N-S extension during the ancient alkaline phase, indicates a change in the regional stress field of Mount Etna through time. The NE-SW and NW-SE direction of magma flow and lateral magma movement of Mount Calanna dykes suggest that, in addition to the continuous N-S extensional stress, the dykes experienced localised tensile stress.

5.3. Emplacement mechanism of the Mount Calanna dyke swarm

Despite of its small size, the Mount Calanna dyke swarm displays a complex dyke injection process with a high intensity of intrusion (40%) (Ferlito and Nicotra, 2010). Two modes of dyke injection are thus found over a very small area, with sub-vertical emplacement lower in the intrusive complex and a sub-horizontal emplacement higher up. This highlights the complex nature of a shallow plumbing system, where the feeder dikes indicate the occurrence of multiple vent openings during the activity of AAC. Such complexity of dyke injection over a small area has also been found at other volcanoes, such as at Lemptegy in central France (Petronis et al., 2013) and Komochi in central Japan (Geshi, 2008). The radial dykes of Komochi exhibit similar dyke flow patterns, characterised by lateral flow from the central conduit and vertical flow from the shallow magma chamber, as found at Mount Calanna. To explain the complexity found at Mount Calanna, at-least two dyke emplacement models are thus needed: one for the emplacement of sub-vertical dykes (e.g., CD1), and one for sub-horizontal dykes (e.g., CD5).

5.3.1. The case of sub-vertical dyke CD1

Characteristic of sub-vertical dykes, CD1 shows a two-stage emplacement mode controlled by both physical (e.g., bedrock strength, regional stress and magma pressure) and fluid (e.g., viscosity, thermal) properties of the country rock and magma, respectively (Lister and Kerr, 1991; Anderson, 1936). During the initial stages of magma injection, the fluid is subjected to controls related to magma pressure and thermal stress due to cooling, and lithostatic forces controlled by the nature of the host rock and shear stress. While the thermal stress and lithostatic forces act laterally towards or away from the flowing magma, the magmatic pressure acts vertically (Fig. 12c). As magma intrudes the host rock, it creates thermal gradients that induce stress in the surrounding rocks. Thermal stress due to cooling, together with the lithostatic forces and simple shear due to the laminar flow of the magma, generates the prolate fabrics (Stage 1 in Fig. 12c). As flow continues, the increased internal pressure causes bending of the NNE side of the dyke (Stage 2 in Fig. 12c) and sagging of the bent side. Sagging, together with the gravity-driven backflow due to its own weight, overprints the initial prolate fabrics with oblate fabrics (Fig. 12b, c) (Andersson et al., 2016; Das et al., 2019).

5.3.2. The case of sub-horizontal dyke CD5

In the case of CD5, which is typical of sub-horizontally emplaced dykes, we observed a different emplacement model with a symmetrical imbrication of the magnetic fabric ellipsoid at the dyke boundary (Fig. 13). The systematic variation of the shape of the AMS ellipsoid across the dyke is expressed by oblate fabrics at the dyke boundaries, but prolate ellipsoids at the dyke centre (Fig. 13b). When magma injects into the country rock, magma at the dyke wall quenches immediately as it comes into contact with the cold country rock. This thus records the initial injection direction. However, near the dyke margin, the inward lithostatic force due to the sudden cooling and the shearing of the magma at the dyke margin results in an oblate ellipsoid (Trippanera et al., 2020). This shearing of magma at the dyke boundary during the intrusion facilities the flattening of the AMS ellipsoid (Roni et al., 2014). (Fig. 13b). At the dyke centre, magma can stay active for days or weeks, even months or years, and the subsequent changes in flow direction, either in the upward or downward directions, causes prolate ellipsoids (Fig. 13b).

6. Conclusion

Interpretation of dyke emplacement is not always straightforward, especially for small dyke swarms which can be easily eroded or covered by subsequent lava flows. However, our work demonstrates how the emplacement dynamics of a small dyke swarm can be unravelled through an interdisciplinary approach involving AMS, fabrics, petrology, and geochemistry, as well as in-field facies analysis.

Our study of the emplacement mechanisms associated with a small intrusive complex provides insights into the flow dynamics and enables us to conclude that:

1. Two distinct groups of dykes are present over a very small area: (a) sub-vertically emplaced dykes which occur in the lower portion of the intrusive complex, and (b) sub-horizontally emplaced dykes in its upper part.
2. We can interpret magma flow directions using the shape of the AMS ellipsoid and imbrication with the dyke wall.
3. There is a dominance of NE-SW flow fabrics for the sub-vertically emplaced dykes, and NE-SW and NW-SE flow directions for the sub-horizontally emplaced dykes; directions which follow the local stress field.
4. The similarity between the field observations and the AMS results suggests that the sub-horizontal dykes migrated laterally from the central conduit to the surface, whereas the sub-vertical dykes were fed by the shallow magma chamber.
5. The palaeomagnetic results together with the geochemical analysis show coeval emplacement of the dykes that make up the swarm.

These observations further suggest that Mount Calanna is an example of the uppermost part of a shallow plumbing system, where patterns in the magnetic fabrics reveal two mode of dyke emplacement in such a system: one for sub-horizontal dykes and a second for sub-vertical dykes. These models show how magma flow is affected by different forces and how flow varies across the dyke within a small intrusion.

The model established here has broad applicability beyond the specific intrusions studied, providing insights into the intricate processes governing dike injection and cooling histories. Furthermore, the stresses controlling the magma flow direction in the flank and central conduit obtained from our AMS results can be integrated with the three-dimensional numerical model for the stress state (Davis et al., 2021; Mantiloni et al., 2023) to simulate dyke propagation pathways in intrusive complexes.

Considering the additional parameters such as rigidity layering, Magma-country rock density ratio and flow rate, following the analogue model experiments of Urbani et al. (2017) can better address the factors driving lateral and vertical dike migration in this small intrusive complex.

CRediT authorship contribution statement

Rasia Shajahan: Conceptualization, Data curation, Methodology, Writing – original draft, Writing – review & editing. **Andrew Harris:** Conceptualization, Formal analysis, Supervision, Writing – review & editing, Writing – original draft. **Sara Mana:** Data curation, Supervision, Writing – original draft, Writing – review & editing. **Eugenio Nicotra:** Investigation, Supervision, Writing – review & editing. **Claudio Robustelli Test:** Data curation, Formal analysis, Investigation, Writing – original draft. **Benjamin van Wyk de Vries:** Data curation, Supervision, Writing – review & editing. **Elena Zanella:** Conceptualization, Data curation, Funding acquisition, Methodology, Supervision, Writing – original draft, Writing – review & editing.

Declaration of competing interest

I, Rasia Shajahan, hereby confirm that the authors involved in this work have no conflict of interest in the subject matter or materials discussed in this manuscript.

Data availability

Data will be made available on request.

Acknowledgements

This project is a part of RS PhD project. This project was funded by MIUR ex-60% attributed to EZ and PhD grants-Budget 10% attributed to RS and CRT. The authors would like to thank Dr. Lorenzo Mantiloni and an anonymous reviewer for their constructive reviews. We also thank Dr. Laura Pioli and Dr. Lucia Gurioli for their early review of this paper, which significantly improved the quality of the manuscript.

Appendix A. Supplementary data

Supplementary data to this article can be found online at https://doi.org/10.1016/j.jvolgeores.2024.108069.

References

Acocella, V., Neri, M., 2009. Dike propagation in volcanic edifices: Overview and possible developments. Tectonophysics 471, 67–77. https://doi.org/10.1016/j.tecto.2008.10.002.
Acocella, V., Neri, M., Scarlato, P., 2006a. Understanding shallow magma emplacement at volcanoes: Orthogonal feeder dikes during the 2002–2003 Stromboli (Italy) eruption. Geophys. Res. Lett. 33, L17310. https://doi.org/10.1029/2006GL026862.
Acocella, Valerio, Porreca, M., Neri, M., Mattei, M., Funiciello, R., 2006b. Fissure eruptions at Mount Vesuvius (Italy): Insights on the shallow propagation of dikes at volcanoes. Geol 34, 673. https://doi.org/10.1130/G22552.1.
Aloisi, M., Bonaccorso, A., Cannavò, F., Gambino, S., Mattia, M., Puglisi, G., Boschi, E., 2009. A new dyke intrusion style for the Mount Etna May 2008 eruption modelled through continuous tilt and GPS data. Terra Nova 21, 316–321. https://doi.org/10.1111/j.1365-3121.2009.00889.x.
Anderson, E.M., 1936. Dynamics of formation of cone-sheets,ring-dikes, and cauldron subsidences. In: Royal Society of Edinburgh Proceedings, 56, pp. 128–157.
Andersson, M., Almqvist, B.S.G., Burchardt, S., Troll, V.R., Malehmir, A., Snowball, I., Kübler, L., 2016. Magma transport in sheet intrusions of the Alnö carbonatite complex, Central Sweden. Sci. Rep. 6, 27635. https://doi.org/10.1038/srep27635.
Archanjo, C.J., Launeau, P., 2004. Magma flow inferred from preferred orientations of plagioclase of the Rio Ceará-Mirim dyke swarm (NE Brazil) and its AMS significance. SP 238, 285–298. https://doi.org/10.1144/GSL.SP.2004.238.01.17.
Bagnardi, M., Amelung, F., Poland, M.P., 2013. A new model for the growth of basaltic shields based on deformation of Fernandina volcano, Galápagos Islands. Earth Planet. Sci. Lett. 377–378, 358–366. https://doi.org/10.1016/j.epsl.2013.07.016.
Balsley, J.R., Buddington, A.F., 1960. Magnetic susceptibility anisotropy and fabric of some Adirondack granites and orthogneisses. Am. J. Sci. 258 (6), e20.
Branca, S., Coltelli, M., De Beni, E., Wijbrans, J., 2008. Geological evolution of Mount Etna volcano (Italy) from earliest products until the first central volcanism (between 500 and 100 ka ago) inferred from geochronological and stratigraphic data. Int. J. Earth Sci. (Geol. Rundsch) 97, 135–152. https://doi.org/10.1007/s00531-006-0152-0.
Branca, S., Coltelli, M., Groppelli, G., Lentini, F., 2011. Geological map of Etna volcano, 1: 50,000 scale. Ital. J. Geosci. 130 (3), 265–291. https://doi.org/10.3301/IJG.2011.15.
Callot, J.P., Guichet, X., 2003. Rock texture and magnetic lineation in dykes: a simple analytical model. Tectonophysics 366, 207–222. https://doi.org/10.1016/S0040-1951(03)00096-9.
Cañón-Tapia, E., 2004. Anisotropy of magnetic susceptibility of lava flows and dykes: a historical account, SP 238, 205–225. https://doi.org/10.1144/GSL.SP.2004.238.01.14.
Chadima, M., Hrouda, F., 2006. Remasoft 3.0 a user-friendly paleomagnetic data browser and analyzer. Travaux Géophysiques 27, 20.
Chadima, M., Jelínek, V., 2008. Anisoft 4.2. – anisotropy data browser. Contrib. Geoph. Geod. 38, 38–41.
Chadima, M., Cajz, V., Týcová, P., 2009. On the interpretation of normal and inverse magnetic fabric in dikes: examples from the Eger Graben, NW Bohemian Massif. Tectonophysics 466, 47–63. https://doi.org/10.1016/j.tecto.2008.09.005.
Corsaro, R.A., Cristofolini, R., 1997. Geology, geochemistry and mineral chemistry of tholeiitic to transitional Etnean magmas. Acta Vulcanol. 9, 55–66.
Coward, M.P., 1980. The analysis of flow profiles in a basaltic dyke using strained vesicles. JGS 137, 605–615. https://doi.org/10.1144/gsjgs.137.5.0605.
Cristofolini, R., Corsaro, R.A., Ferlito, C., 1991. Variazioni petrochimiche nella successione etnea: un riesame in base a nuovi dati da campioni di superficie e da sondaggi. Acta Vulcanol. 1, 25–37.
Daniels, K.A., Menand, T., 2015. An experimental investigation of dyke injection under regional extensional stress. J. Geophys. Res. Solid Earth 120, 2014–2035. https://doi.org/10.1002/2014JB011627.
Das, A., Mallik, J., 2020. Applicability of AMS technique as a flow fabric indicator in dykes: insight from Nandurbar–Dhule Deccan dyke swarm. Int. J. Earth Sci. (Geol. Rundsch) 109, 933–944. https://doi.org/10.1007/s00531-020-01841-9.
Das, A., Mallik, J., Bandyopadhyay, K., Alam, R., 2019. A review of anisotropy of magnetic susceptibility analysis of Indian dykes: Implications for magma emplacement. IJES 11. https://doi.org/10.30495/ijes.2019.544593.
Das, A., Mallik, J., Banerjee, S., 2021. Characterization of the magma flow direction in the Nandurbar-Dhule Deccan dyke swarm inferred from magnetic fabric analysis. Phys. Earth Planet. Inter. 319, 106782 https://doi.org/10.1016/j.pepi.2021.106782.
Datta, S., Banerjee, S., Samal, A.K., Srivastava, R.K., 2023. Aspect ratio analysis of distinct Paleoproterozoic mafic dyke swarms and related fracture systems in the Eastern Dharwar Craton, India: Implications for emplacement mechanism and depth of origin. Phys. Earth Planet. Inter. 336, 106998 https://doi.org/10.1016/j.pepi.2023.106998.

Davis, T., Bagnardi, M., Lundgren, P., Rivalta, E., 2021. Extreme Curvature of Shallow Magma Pathways Controlled by competing Stresses: Insights from the 2018 Sierra Negra Eruption. Geophys. Res. Lett. 48 https://doi.org/10.1029/2021GL093038 e2021GL093038.

De Beni, E., Branca, S., Coltelli, M., Groppelli, G., Wijbrans, J.R., 2011. 40Ar/39Ar isotopic dating of Etna volcanic succession. Ital. J. Geosci. 292–305 https://doi.org/10.3301/IJG.2011.14.

Decker, R.W., 1987. Dynamics of Hawaiian volcanoes: an overview. US Geol. Surv. Prof. Pap. 1350, 997–1018.

Delcamp, A., Petronis, M.S., Troll, V.R., 2015. Discerning magmatic flow patterns in shallow-level basaltic dykes from the NE rift zone of Tenerife, Spain, using the Anisotropy of magnetic Susceptibility (AMS) technique. SP 396, 87–106. https://doi.org/10.1144/SP396.2.

Dragoni, M., Lanza, R., Tallarico, A., 1997. Magnetic anisotropy produced by magma flow: theoretical model and experimental data from Ferrar dolerite sills (Antarctica). Geophys. J. Int. 128, 230–240. https://doi.org/10.1111/j.1365-246X.1997.tb04083.x.

Eriksson, P.I., Riishuus, M.S., Elming, S.-Å., 2015. Magma flow and palaeo-stress deduced from magnetic fabric analysis of the Álftafjörður dyke swarm: implications for shallow crustal magma transport in Icelandic volcanic systems. SP 396, 107–132. https://doi.org/10.1144/SP396.6.

Ernst, R.E., Baragar, W.R.A., 1992. Evidence from magnetic fabric for the flow pattern of magma in the Mackenzie giant radiating dyke swarm. Nature 356, 511–513. https://doi.org/10.1038/356511a0.

Ferlito, C., Nicotra, E., 2010. The dyke swarm of Mount Calanna (Etna, Italy): an example of the uppermost portion of a volcanic plumbing system. Bull. Volcanol. 72, 1191–1207. https://doi.org/10.1007/s00445-010-0398-z.

Ferrari, L., Calvari, S., Coltelli, M., Innocenti, F., Pasquarè, G., Pompilio, M., Vezzoli, L., Villa, I., 1989. Nuovi dati geologici e strutturali sulla Valle di Calanna, Etna: implicazioni per l'evoluzione del vulcanismo etneo. Boll. GNV 2, 849–860.

Fisher, R., 1953. Dispersion on a Sphere. In: Proceedings of the Royal Society A: Mathematical, Physical and Engineering Sciences, 217, pp. 295–305. https://doi.org/10.1098/rspa.1953.0064.

Francis, P., 1993. Volcanoes. A Planetary Perspective., Volcanoes. A Planetary Perspective.

Gautneb, H., Gudmundsson, A., 1992. Effect of local and regional stress fields on sheet emplacement in West Iceland. J. Volcanol. Geotherm. Res. 51, 339–356. https://doi.org/10.1016/0377-0273(92)90107-O.

Geoffroy, L., Callot, J.P., Aubourg, C., Moreira, M., 2002. Magnetic and plagioclase linear fabric discrepancy in dykes: a new way to define the flow vector using magnetic foliation. Terra Nova 14, 183–190. https://doi.org/10.1046/j.1365-3121.2002.00412.x.

Geshi, N., 2008. Vertical and lateral propagation of radial dikes inferred from the flow-direction analysis of the radial dike swarm in Komochi Volcano, Central Japan. J. Volcanol. Geotherm. Res. 173, 122–134. https://doi.org/10.1016/j.jvolgeores.2008.01.001.

Gillot, P.Y., Kieffer, G., Romano, R., 1994. The evolution of Mount Etna in the light of potassium-argon dating. Acta Vulcanol. 5, 81–87.

Gudmundsson, A., 1990. Emplacement of dikes, sills and crustal magma chambers at divergent plate boundaries. Tectonophysics 176, 257–275. https://doi.org/10.1016/0040-1951(90)90073-H.

Gudmundsson, A., 2002. Emplacement and arrest of sheets and dykes in central volcanoes. J. Volcanol. Geotherm. Res. 116, 279–298. https://doi.org/10.1016/S0377-0273(02)00226-3.

Gvirtzman, Z., Nur, A., 1999. The formation of Mount Etna as the consequence of slab rollback. Nature 401, 782–785. https://doi.org/10.1038/44555.

Hamling, I.J., Wright, T.J., Calais, E., Bennati, L., Lewi, E., 2010. Stress transfer between thirteen successive dyke intrusions in Ethiopia. Nat. Geosci. 3, 713–717. https://doi.org/10.1038/ngeo967.

Hext, G.R., 1963. The estimation of second-order tensors, with related tests and designs. Biometrika 50, 353–373. https://doi.org/10.1093/biomet/50.3-4.353.

Hoyer, L., Watkeys, M.K., 2017. Using magma flow indicators to infer flow dynamics in sills. J. Struct. Geol. 96, 161–175. https://doi.org/10.1016/j.jsg.2017.02.005.

Hrouda, F., 1982. Magnetic anisotropy of rocks and its application in geology and geophysics. Geophys. Surv. 5, 37–82. https://doi.org/10.1007/BF01450244.

Hughes, J.W., 1990. Changing styles of effusive eruption on Mount Etna since AD 1600. Magma Transp. Storag. 385–406.

Jelinek, V., 1981. Characterization of the magnetic fabric of rocks. Tectonophysics 79, T63–T67. https://doi.org/10.1016/0040-1951(81)90110-4.

Jochum, K.P., Weis, U., Schwager, B., Stoll, B., Wilson, S.A., Haug, G.H., Andreae, M.O., Enzweiler, J., 2016. Reference Values following ISO guidelines for frequently Requested Rock Reference Materials. Geostand. Geoanal. Res. 40, 333–350. https://doi.org/10.1111/j.1751-908X.2015.00392.x.

Khan, M.A., 1962. The anisotropy of magnetic susceptibility of some igneous and metamorphic rocks. J. Geophys. Res. 67, 2873–2885. https://doi.org/10.1029/JZ067i007p02873.

Klerkx, J., 1970. La caldera de la Valle del Bove: sa signification dans l'évolution de l'Etna (Sicile). Bull. Volcanol. 34, 726–737. https://doi.org/10.1007/BF02596701.

Knight, M.D., Walker, G.P.L., 1988. Magma flow directions in dikes of the Koolau complex, Oahu, determined from magnetic fabric studies. J. Geophys. Res. 93, 4301–4319. https://doi.org/10.1029/JB093iB05p04301.

Le Maitre, R.W., Streckeisen, A., Zanettin, B., Le Bas, M.J., Bonin, B., Bateman, P. (Eds.), 2002. Igneous Rocks: A Classification and Glossary of Terms, 2nd ed. Cambridge University Press, Cambridge. https://doi.org/10.1017/CBO9780511535581.

Lister, J.R., Kerr, R.C., 1991. Fluid-mechanical models of crack propagation and their application to magma transport in dykes. J. Geophys. Res. 96, 10049. https://doi.org/10.1029/91JB00600.

Lo Giudice, E., Patanè, G., Rasà, R., Romano, R., 1982. The structural framework of Mount Etna. Mem. Soc. Geol. Ital. 23, 125–158.

Lowrie, W., 1990. Identification of ferromagnetic minerals in a rock by coercivity and unblocking temperature properties. Geophys. Res. Lett. 17, 159–162. https://doi.org/10.1029/GL017i002p00159.

Maccaferri, F., Bonafede, M., Rivalta, E., 2011. A quantitative study of the mechanisms governing dike propagation, dike arrest and sill formation. J. Volcanol. Geotherm. Res. 208, 39–50. https://doi.org/10.1016/j.jvolgeores.2011.09.001.

Maccaferri, F., Richter, N., Walter, T.R., 2017. The effect of giant lateral collapses on magma pathways and the location of volcanism. Nat. Commun. 8, 1097. https://doi.org/10.1038/s41467-017-01256-2.

Magee, C., Stevenson, C.T.E., Ebmeier, S.K., Keir, D., Hammond, J.O.S., Gottsmann, J.H., Whaler, K.A., Schofield, N., Jackson, C.A.-L., Petronis, M.S., O'Driscoll, B., Morgan, J., Cruden, A., Vollgger, S.A., Dering, G., Micklethwaite, S., Jackson, M.D., 2018. Magma Plumbing Systems: a Geophysical Perspective. J. Petrol. 59, 1217–1251. https://doi.org/10.1093/petrology/egy064.

Mantiloni, L., Rivalta, E., Davis, T., 2023. Mechanical Modeling of Pre-Eruptive Magma Propagation scenarios at Calderas. JGR Solid Earth 128. https://doi.org/10.1029/2022JB025956 e2022JB025956.

Martin, S.A., Kavanagh, J.L., Biggin, A.J., Utley, J.E.P., 2019. The Origin and Evolution of magnetic Fabrics in Mafic Sills. Front. Earth Sci. 7, 64. https://doi.org/10.3389/feart.2019.00064.

Maxbauer, D.P., Feinberg, J.M., Fox, D.L., 2016. MAX UnMix: a web application for unmixing magnetic coercivity distributions. Comput. Geosci. 95, 140–145. https://doi.org/10.1016/j.cageo.2016.07.009.

McDonough, W.F., Sun, S.-S., 1995. The composition of the Earth. Chem. Geol. 120, 223–253. https://doi.org/10.1016/0009-2541(94)00140-4.

McGuire, W.J., 1982. Evolution of the Etna volcano: Information from the southern wall of the Valle Del Bove Caldera. J. Volcanol. Geotherm. Res. 13, 241–271. https://doi.org/10.1016/0377-0273(82)90053-1.

McGuire, W.J., Pullen, A.D., 1989. Location and orientation of eruptive fissures and feederdykes at Mount Etna; influence of gravitational and regional tectonic stress regimes. J. Volcanol. Geotherm. Res. 38, 325–344. https://doi.org/10.1016/0377-0273(89)90046-2.

Minakov, A., Yarushina, V., Faleide, J.I., Krupnova, N., Sakoulina, T., Dergunov, N., Glebovsky, V., 2018. Dyke emplacement and crustal structure within a continental large igneous province, northern Barents Sea. SP 460, 371–395. https://doi.org/10.1144/SP460.4.

Monaco, C., Tapponnier, P., Tortorici, L., Gillot, P.Y., 1997. Late Quaternary slip rates on the Acireale-Piedimonte normal faults and tectonic origin of Mt. Etna (Sicily). Earth Planet. Sci. Lett. 147, 125–139. https://doi.org/10.1016/S0012-821X(97)00005-8.

Monaco, C., Catalano, S., Cocina, O., De Guidi, G., Ferlito, C., Gresta, S., Musumeci, C., Tortorici, L., 2005. Tectonic control on the eruptive dynamics at Mt. Etna Volcano (Sicily) during the 2001 and 2002–2003 eruptions. J. Volcanol. Geotherm. Res. 144, 211–233. https://doi.org/10.1016/j.jvolgeores.2004.11.024.

Nagata, T., 1961. Rock magnetism, Maruzen, Tokyo. Nnange, J. Mining, Poudjom Djomani, p. 350.

Nicotra, E., Viccaro, M., 2012. Unusual magma storage conditions at Mt. Etna (Southern Italy) as evidenced by plagioclase megacryst-bearing lavas: implications for the plumbing system geometry and summit caldera collapse. Bull. Volcanol. 74, 795–815. https://doi.org/10.1007/s00445-011-0566-9.

Nicotra, E., Viccaro, M., Ferlito, C., Cristofolini, R., 2010. Influx of volatiles into shallow reservoirs at Mt. Etna volcano (Italy) responsible for halogen-rich magmas. ejm 22, 121–138. https://doi.org/10.1127/0935-1221/2010/0022-1991.

Nicotra, E., Ferlito, C., Viccaro, M., Cristofolini, R., 2011. Volcanic geology and petrology of the Val Calanna succession (Mt. Etna, Southern Italy): discovery of a new eruptive center. Periodico di Mineral. 80, 287–307. https://doi.org/10.2451/2011PM0021.

Otmane, K., Errami, E., Olivier, P., Berger, J., Triantafyllou, A., Ennih, N., 2018. Magnetic fabric and flow direction in the Ediacaran Imider dyke swarms (Eastern Anti-Atlas, Morocco), inferred from the Anisotropy of magnetic Susceptibility (AMS). J. Afr. Earth Sci. 139, 55–72. https://doi.org/10.1016/j.jafrearsci.2017.11.030.

Pansino, S., Taisne, B., 2019. How Magmatic Storage Regions Attract and Repel Propagating Dikes. JGR Solid Earth 124, 274–290. https://doi.org/10.1029/2018JB016311.

Petronis, M.S., Delcamp, A., Van Wyk De Vries, B., 2013. Magma emplacement into the Lemptégy scoria cone (Chaîne Des Puys, France) explored with structural, anisotropy of magnetic susceptibility, and Paleomagnetic data. Bull. Volcanol. 75, 753. https://doi.org/10.1007/s00445-013-0753-y.

Philpotts, A.R., Dickson, L.D., 2000. The formation of plagioclase chains during convective transfer in basaltic magma. Nature 406, 59–61. https://doi.org/10.1038/35017542.

Pinel, V., Carrara, A., Maccaferri, F., Rivalta, E., Corbi, F., 2017. A two-step model for dynamical dike propagation in two dimensions: Application to the July 2001 Etna eruption. JGR Solid Earth 122, 1107–1125. https://doi.org/10.1002/2016JB013630.

Raposo, M.I.B., Ernesto, M., 1995. Anisotropy of magnetic susceptibility in the Ponta Grossa dyke swarm (Brazil) and its relationship with magma flow direction. Phys. Earth Planet. Inter. 87, 183–196. https://doi.org/10.1016/0031-9201(94)02970-M.

Rasband, W.S., 2012. ImageJ: image processing and analysis in Java. In: Astrophysics Source Code Library (ascl:1206.013).

Ray, R., Sheth, H.C., Mallik, J., 2007. Structure and emplacement of the Nandurbar–Dhule mafic dyke swarm, Deccan Traps, and the tectonomagmatic

evolution of flood basalts. Bull. Volcanol. 69, 537–551. https://doi.org/10.1007/s00445-006-0089-y.
Rivalta, E., Taisne, B., Bunger, A.P., Katz, R.F., 2015. A review of mechanical models of dike propagation: Schools of thought, results and future directions. Tectonophysics 638, 1–42. https://doi.org/10.1016/j.tecto.2014.10.003.
Rochette, P., Jackson, M., Aubourg, C., 1992. Rock magnetism and the interpretation of anisotropy of magnetic susceptibility. Rev. Geophys. 30, 209. https://doi.org/10.1029/92RG00733.
Roman, A., Jaupart, C., 2014. The impact of a volcanic edifice on intrusive and eruptive activity. Earth Planet. Sci. Lett. 408, 1–8. https://doi.org/10.1016/j.epsl.2014.09.016.
Romano, R., 1982. Succession of the volcanic activity in the Etnean area. Mem. Soc. Geol. Ital. 23, 27–48.
Romano, R., Sturiale, Carmelo, 1975. Geologia della Tavoletta" Monte Etna sud"(F. 262-III SO). Boll. Soc. Geol. Ital. 94 (5), 1109–1148.
Roni, E., Westerman, D.S., Dini, A., Stevenson, C., Rocchi, S., 2014. Feeding and growth of a dyke–laccolith system (Elba Island, Italy) from AMS and mineral fabric data. JGS 171, 413–424. https://doi.org/10.1144/jgs2013-019.
Schmiedel, T., Burchardt, S., Mattsson, T., Guldstrand, F., Galland, O., Palma, J., Skogby, H., 2021. Emplacement and Segment Geometry of large, High-Viscosity Magmatic Sheets. Minerals 11, 1113. https://doi.org/10.3390/min11101113.
Stacey, F.D., Joplin, G., Lindsay, J., 1960. Magnetic anisotropy and fabric of some foliated rocks from S.E. Australia. Geofisica Pura e Appl. 47, 30–40. https://doi.org/10.1007/BF01992481.
Tanguy, J.-C., Condomines, M., Kieffer, G., 1997. Evolution of the Mount Etna magma: Constraints on the present feeding system and eruptive mechanism. J. Volcanol. Geotherm. Res. 75, 221–250. https://doi.org/10.1016/S0377-0273(96)00065-0.
Tarling, D., Hrouda, F. (Eds.), 1993. Magnetic Anisotropy of Rocks. Springer Science & Business Media.
Trippanera, D., Porreca, M., Urbani, S., Kissel, C., Winkler, A., Sagnotti, L., Nazzareni, S., Acocella, V., 2020. Interpreting Inverse magnetic fabric in Miocene Dikes from Eastern Iceland. JGR Solid Earth 125. https://doi.org/10.1029/2020JB020306 e2020JB020306.
Urbani, S., Acocella, V., Rivalta, E., Corbi, F., 2017. Propagation and arrest of dikes under topography: Models applied to the 2014 Bardarbunga (Iceland) rifting event. Geophys. Res. Lett. 44, 6692–6701. https://doi.org/10.1002/2017GL073130.
Weaver, R., Roberts, A.P., Barker, A.J., 2002. A late diagenetic (syn-folding) magnetization carried by pyrrhotite: implications for paleomagnetic studies from magnetic iron sulphide-bearing sediments. Earth Planet. Sci. Lett. 200, 371–386. https://doi.org/10.1016/S0012-821X(02)00652-0.
Wiegand, M., Trumbull, R.B., Kontny, A., Greiling, R.O., 2017. An AMS study of magma transport and emplacement mechanisms in mafic dykes from the Etendeka Province, Namibia. Tectonophysics 716, 149–167. https://doi.org/10.1016/j.tecto.2016.08.016.
Wing-Fatt, L., Stacey, F.D., 1966. Magnetic anisotropy of laboratory materials in which magma flow is simulated. Pageoph 64, 78–80. https://doi.org/10.1007/BF00875533.
Woo, J.Y.L., Kilburn, C.R.J., 2010. Intrusion and deformation at Campi Flegrei, southern Italy: Sills, dikes, and regional extension. J. Geophys. Res. 115, B12210. https://doi.org/10.1029/2009JB006913.